Time-resolved bottleneck analysis in bacterial infection dynamics

Sylvain Vicente[1]* (ID), Nathanaël Boutillon[2,3,4] (ID), Raphael Forien[2] (ID), Isabelle Mila[1] (ID), Lionel Roques[2] (ID), and Nemo Peeters[1]* (ID)

[1] *Université de Toulouse, INRAE, CNRS, LIPME, Castanet-Tolosan, France*

[2] *INRAE, BioSP, Avignon 84914, France*

[3] *Aix Marseille Université, CNRS, I2M, Marseille, France*

[4] *Faculty of Mathematics, University of Vienna, Oskar-Morgenstern-Platz 1, Wien, 1090, Austria*

[*] *Correspondence: sylvain.vicente@inrae.fr, nemo.peeters@inrae.fr*

2025/11/20

Abstract

Within-host pathogen dynamics can be difficult to track, involving pathogen expansions and restrictions by host barriers bottlenecks, ultimately determining the outcome of the infection. We use a neutral barcoding approach to monitor the root entry bottleneck during infections of tomato plants *Solanum lycopersicum* by the bacterial phytopathogen *Ralstonia pseudosolanacearum*. In our context, classical bottleneck analyses frameworks showed to be poorly accurate. By investigating data with novel bottleneck models, we conclude that the overlooked time dimension is crucial to understand root colonisation but also allows the resolution of previously inaccessible infection metrics. We define a new type of "time-resolved" bottlenecks describing infection scenarios where entry of pathogen occurs continuously with growth of pathogen in the host. Application of the "time-resolved" bottleneck framework to two published animal infection datasets confirms that it is not host-specific but may provide new conceptual understanding to many experimental studies that assumed bottlenecks to be instantaneous.

Understanding the spatio-temporal dynamics of pathogens within hosts is key to explaining infection success. The molecular interactions between the host and the pathogen, and eventually the colonisation, growth, and motility within the host can be integrated at the individual host level by monitoring the genetic structure of the pathogen population. More generally, while significant research is dedicated to understanding the molecular mechanisms of bacterial pathogens virulence, acquiring both quantitative and descriptive metrics of an infection can be challenging. The STAMP (Sequence Tag-Based Analysis of Microbial Population) framework[1] and its extensions[2,3] have been particularly effective in monitoring the dynamics of the infecting population and identifying bottlenecks in different host-bacterial pathosystems. The general objectives of this type of approach include pinpointing the locations of host barriers, quantifying the strength of these barriers against pathogens and ultimately, attempt to predict the survival or death outcome of a host in a given condition.

STAMP introduces neutral genetic diversity by inserting short sequence tags into the pathogen genome. The artificially tagged population mimics a wild-type population, in which the introduced neutral diversity serves as a recorder of the genetic history of the infectious population. A key use of this method is the identification of infectious bottleneck events during infection, when the pathogen population undergoes a strong reduction in size, which can be quantified by a subsequent drop in neutral diversity. The bottleneck was originally defined as *number of founding pathogen cells* that cross the barrier and expand[1]. Although many studies have now been published using this type of indicators[2,3,4,5,6,7,8,9,10,11,12,13,14,15,16,17], the question of the link between diversity patterns measured through STAMP and the nature of the underlying population genetics processes remains unaddressed.

Ralstonia pseudosolanacearum is a soil-borne phytopathogen responsible for bacterial wilt, a devastating disease of solanaceous crops such as tomato and potato. The bacterium invades plant roots and rapidly colonises the xylem, causing vascular occlusion, followed by wilting and plant death. Previous studies have identified localised barriers to infection, including physical defences in the root[18]. Microscopy of early infection typically shows pathogen entry through the root epidermis, colonisation across cell layers and eventually penetration into the xylem where the pathogen thrives[18,19,20,21].

To quantify the root-entry bottleneck underlying these observations, we infected tomato plants with a collection of 120 neutral genetic barcodes in *R. pseudosolanacearum*. Pathogen colonisation was analysed using the original STAMP framework[1] and its algorithmically corrected version, STAMPR[2]. A stringent entry bottleneck was detected with losses of neutral barcodes during roots infection. Although both frameworks detected this bottleneck, they failed to capture the fine-scale patterns of root colonisation. By addressing a key theoretical gap, we show that the standard definition of a "bottleneck"—as the number of founding pathogen cells—is valid only under a restricted scenario where bacterial entry is decoupled from subsequent growth or migration. We term this the *instantaneous bottleneck model* (or *STAMP model*). In contrast, our data and reanalysis of prior studies support a scenario in which bottlenecks occur concurrently with growth and migration. We define this concept as the *time-resolved bottleneck model*, governed by time-dependent population dynamics.

To formalise this view, we introduce three complementary *time-resolved models* grounded in popu-

lation genetics. Each fits our data better than the instantaneous bottleneck model (STAMP) and aligns with our understanding of the physiology of *R. pseudosolanacearum* infection. Reanalyses of published animal datasets[5,13] reveal analogous dynamics in *Pseudomonas aeruginosa* and *Klebsiella pneumoniae* infections in mice. The framework better exploits information contained in diversity profile structure, yielding updated metrics that refine bottleneck estimates and resolve time-dependent parameters, particularly in experimental cases where a single bottleneck value is inadequate. The integrality of results and the associated methods are made available through a fully annotated computational document in R, ensuring the reproducibility of the approach for the analysis of neutral barcoding experiments.

1 Results

1.1 Physical barriers in plant roots impose a stringent pathogen-limiting bottleneck

To understand the dynamics of *Ralstonia pseudosolanacearum* infection, we applied the neutral barcoding approach STAMP[1] to our plant–pathogen system (Fig. 1a). The reference strain GMI1000 was barcoded by inserting a 20 bp polymorphic tag in a known neutral intergenic chromosomal locus[22]. 119 tagged strains were validated and showed comparable growth *in vitro* (Fig. S1). In co-culture, the proportions of the 119 tags remained stable (Fig. S1), indicating that preparation steps did not introduce technical bottlenecks, that tagged strains exhibited indistinguishable *in vitro* growth, and that sequencing did not introduce appreciable PCR bias. The co-cultures were used as inoculum for plant infections.

We next asked whether root defences constitute a population-limiting barrier to *R. pseudosolanacearum*. We formulated four predictions: (*i*) if a root-entry bottleneck exists, tag diversity will decrease after root colonisation; (*ii*) with subsequent expansion, diversity should stabilise over time; (*iii*) bottleneck magnitude should depend on root integrity; and (*iv*) if all tagged strains have equal fitness, all tags should have identical probability to appear across independent infections.

Susceptible tomato plants (*cv.* Marmande) were inoculated with the tagged co-culture sampled between 2-6 days post-inoculation (DPI). Each day, whole taproots were collected for colony-forming unit (CFU) quantification (Fig. 1b) and tag sequencing to compute Shannon diversity (Fig. 1c). Bacterial loads increased over time, consistent with growth and progressive colonisation. In parallel, the average Shannon diversity converged to ~ 2 by 4-6 DPI, indicating rapid establishment of a stable pathogen diversity. Sampling time had little effect on diversity once colonisation was established. Importantly, *in planta* diversity was consistently lower than in the inoculum, demonstrating a root-entry bottleneck. The 119-tag collection reliably captured population reduction, suggesting that unconstrained entry is unlikely and that collection complexity is sufficient to understand bottleneck effects in this context. Diversity profiles indicated losses in both richness (tag extinction) and evenness (frequency imbalance) (Fig. 1d).

To test whether physical root barriers underlie the bottleneck, we performed a second experiment comparing intact roots with roots-scarified plants, cut immediately prior to inoculation. Control Marmande tomato plants were infected as above with the 119-tag co-culture. For each condition, three replicates of $n = 8$ plants were harvested at the onset of first symptoms within each batch (Fig. S2), balancing sequencing of sufficient amount of bacterial DNA with representation of pathogen growth dynamics. Root samples were processed for CFU and diversity (Figs. 2a,2b,2c). Control intact Marmande tomato plants had a behaviour similar to the plants in the first experiment, both in CFU and diversity. By contrast, cut roots showed a significant increase in entry diversity (Fig. 2d), demonstrating that root physical integrity contributes to the root-entry bottleneck. This quantitative result aligns with qualitative reports showing that root structure impedes early infection[18,19,20,21].

Finally, we assessed the neutral-fitness assumption. No tag showed consistent over-representation across infections (Fig. S3), indicating that tagged strains have similar probabilities of establishing infection. Thus, the observed diversity profiles reflect pathogen entry dynamics at the root rather than tag-specific fitness effects or technical artifacts such as sequencing bias.

1.2 Diversity profiles encode previously unexploited information about the pathogen's mode of entry

Observed diversity profiles are inconsistent with STAMP/STAMPR frameworks. As a first approach, we quantified the root-entry bottleneck using published metrics. We computed the standard bottleneck metric N_b from the original STAMP framework[1] and the corrected (N_r) and simulated (N_s) bottlenecks from STAMPR[2]. These related metrics all interpret a bottleneck as a "number of founding pathogen cells". To assess robustness, we compared each estimate with the sample richness R—the minimum number of founders required to account for the observed tags R in samples (Fig. 3a).

Median richness was $R \approx 30$ tags in intact plants and $R \approx 110$ in cut-root plants. N_b performed poorly, strongly underestimating entry in view of observed tags (intact: median $N_b \approx 3$; cut: median $N_b \approx 14$). N_r tracked richness more closely (intact: median $N_r \approx 12$; cut: median $N_r \approx 300$), whereas N_s systematically failed (intact: median $N_s \approx 2$; cut: median $N_s \approx 1$), consistent with known limitations of N_s for small collections and stringent bottlenecks[2].

As the most coherent estimator, N_r is an algorithmic correction rather than a mechanistic estimator with an explicit model. It is difficult to quantify its robustness beyond empirical checks. Nevertheless, we assessed the ability of N_r to account for tags within individual samples (Fig. 3b). Most intact-root plants (14 out of 17) and several cut-root plants (6 out of 24) had $N_r < R$ indicating that systematic discrepancies were also common in N_r below a richness threshold of ~ 60 tags.

Inspection of individual diversity profiles (Figs. S4) showed further inconsistencies in N_b and N_r which only take into account high-frequency tags while ignoring low-frequency tags. Critically, observed tag frequencies formed continuous gradients rather than one or more flat tiers, inconsistent with the

idea that the population could originate from finite low numbers of founders.

These discrepancies prompted us to question the adequacy of N_b-derived indicators in this infection context. Notably, the N_b equation[1] and its derivatives N_r and N_s[2] lack an explicit mechanistic framework demonstrating that a bottleneck defined as a "number of founders" reflects the underlying biological mechanisms. In population genetics, such a definition implicitly invokes a founder event as a single, instantaneous transition separating two non-overlapping populations[23,24]—an *instantaneous bottleneck model* (the *STAMP model*), where infection barrier crossing is decoupled from subsequent growth (Fig. 3c). This interpretation relies on four implicit assumptions[23]: (1) Neutral diversity: all tags have identical fitness for growth and virulence; (2) Compartmentalised space: soil and root are distinct compartments; (3) Spatial homogeneity: all soil tags have equal access to roots; tissue complexity is ignored. (4) Instantaneous barrier: a single, instantaneous entry with no secondary infections.

Assumptions (1) and (2) are supported by our knowledge of the infection and the verification of the neutral tags collection. By contrast, (3) and (4) remain untested in the literature and are likely false in our system because experimentally observed contributions of motility and growth to colonisation[18,19,20,21] are neglected in the N_b.

STAMPR was proposed to mitigate N_b's shortcomings by accommodating either multiple simultaneous entries or a single entry that yields differentially growing subpopulations, producing N_r and N_s[2]. Empirically, this corresponds to a "multiple instantaneous bottlenecks" interpretation (Fig. 3d). However, this approach still requires that the infectious population comprises k discrete subpopulations and that each subpopulation satisfies the four assumptions inherited from STAMP. Violations of assumptions (3) or (4) therefore propagate to STAMPR.

Investigating time-dependent effects is necessary for a better understanding of pathogen colonisation. Unlike non-parametric summaries (*e.g.*, Shannon diversity, richness), bottleneck estimators such as N_b and N_r rely on the validity of their underlying models. Because no rigorous validation tools were provided for assumptions (3) and (4), alternative models may better explain our data. This particularly applies to time-dependent biological effects such as dissemination, growth or spatial occupation effects that cannot be investigated under STAMP(-R).

Prior work suggests that *R. pseudosolanacearum* entry is a continuous influx rather than a single event[18,19,20,21]. If entry and growth proceed concurrently, prior entering bacteria should, on average, reach higher frequencies than those entering later. We therefore define a class of *time-resolved* bottleneck models in which entry overlaps in time with expansion. To challenge the STAMP paradigm, we develop three alternatives from distinct population genetics perspectives:

- **Constant-entry-rate model** ($\mathcal{M}_{\mathrm{CR}}$): pathogen cells enter the roots at a constant rate and then grow exponentially (Fig. 3e).
- **Bolthausen-Sznitman model** ($\mathcal{M}_{\mathrm{BS}}$): root colonisation is treated as a stochastic range expansion that simulates the diffusion and spatial occupation of pathogen inside the root. The

genealogies in the range expansion follow a Bolthausen-Sznitman coalescent[25] (Fig. 3f).

- **Increasing-entry-rate model** ($\mathcal{M}_{\mathrm{IR}}$): a generalisation of $\mathcal{M}_{\mathrm{CR}}$ with exponentially increasing entry rates over time; established cells grow exponentially. This model reproduces the progressive breaching of the host's defensive barriers observed in $\mathcal{M}_{\mathrm{BS}}$ (Fig. S5), and has a simpler mechanistic interpretation. (Fig. 3g).

1.3 A model-testing approach reveals new biological insights into *in planta* infection dynamics

We introduce a procedure for analysing neutral barcoding data that treats the within-host pathogen diversity profile structure as an informative signature of the infection dynamics. The rationale is straightforward: if diversity profiles record the mode of entry, then the most plausible bottleneck mechanism can be inferred by comparing observed profiles to those predicted by mechanistic models. For each sample, we simulate tag-frequency distributions under four models—$\mathcal{M}_{\mathrm{STAMP}}, \mathcal{M}_{\mathrm{CR}}, \mathcal{M}_{\mathrm{BS}}, \mathcal{M}_{\mathrm{IR}}$—and optimise model parameters to best match the empirical diversity structure (Fig. 4a). Model fit is assessed by minimising the discrepancy between the sample's Hill-number curve and the simulated Hill-number curve. Critically, a diversity profile is characterised by its Hill-number curve[26].

Figure 4b shows Hill-number curves for the best-fitting simulation under each model. As a guide, $q = 0$ equals richness R, $q = 1$ is the exponential of Shannon entropy (also known as "Shannon diversity"), and $q = 2$ is the inverse Simpson index (also known as "Simpson diversity"). Low q values emphasise rare tags, whereas higher q values emphasise dominant tags, allowing Hill numbers to jointly describe both the number and relative balance of tags frequencies.

For example, in intact Marmande tomato plants, curves span low-to-high richness values at $q = 0$, and decline with increasing q. Steeper drops indicate greater unevenness in tags frequencies. We quantify model accuracy by an error score—the deviation between observed and simulated Hill-number curves—computed across all samples (Fig. 4c) and by condition (Fig. S6). $\mathcal{M}_{\mathrm{STAMP}}$ was consistently unable to catch diversity of low frequency tags. All time-resolved models improved fit, with $\mathcal{M}_{\mathrm{BS}}$ and $\mathcal{M}_{\mathrm{IR}}$ providing the closest matches, jointly capturing equilibrium among dominant tags and the persistence of numerous low-frequency tags, and corresponding well to the observed Hill-number curve.

This model-testing framework directly addresses the nature of the bottleneck. The general failure of $\mathcal{M}_{\mathrm{STAMP}}$ to reproduce observed diversity argues against an instantaneous bottleneck in our system. Instead, diversity profiles support a process driven by continuous entry of pathogens into roots, reflected by uniformly lower error scores for the three time-resolved models.

A second set of conclusions concerns the nature of the time-resolved bottleneck. $\mathcal{M}_{\mathrm{BS}}$ and $\mathcal{M}_{\mathrm{IR}}$ outperform $\mathcal{M}_{\mathrm{CR}}$ at low orders ($q \leq 2$) for the detection of low-frequency tags. The principal difference is the mode of entry: $\mathcal{M}_{\mathrm{CR}}$ assumes a constant entry rate, whereas $\mathcal{M}_{\mathrm{BS}}$ and $\mathcal{M}_{\mathrm{IR}}$ imply an accelerating rate of entry over time (Fig. S5). Two implications follow. First, low-frequency tags are expected under a time-resolved bottleneck and are not mere artefacts. One explanation for the better performance of

$\mathcal{M}_{\mathrm{BS}}$ could be its ability to simulate preservation of rare lineages[25]. Even with little to no growth or extreme bottlenecks, minor secondary infections may occur and persist. Second, root permeability to the pathogen likely increases during infection, indicating potential weakening of host defences. This result is also coherent with observation of plasmolysis of cortical cells during infection[19,20,21] because widening a direct access to the xylem would mechanically decrease the entry barrier in the plant.

1.4 Time-resolved bottleneck quantifies plant susceptibility or tolerance

To broaden inference, we added infections spanning three factors: *root condition* (intact *vs.* cut), *plant genotype* (susceptible *cv.* Marmande *vs.* tolerant *cv.* Hawaii7996[21,27,28]), and *temperature* (27 °C *vs.* 32 °C) (Fig. 5a). Eight conditions were generated, including the two baselines of intact or cut Marmande tomato plants infected at 27°C (*M_Intact_27*, *M_Cut_27*) from Fig. 2. Sampling followed symptom onset as described in Materials and Methods.

All these factors are known to alter disease progression. Susceptibility-promoting modalities (Marmande tomato plants, cut roots, 32 °C, noted *M_Cut_32*) led to earlier symptoms, higher CFU, and earlier sampling (Fig. S2). Conversely, tolerant modalities (Hawaii7996 tomato plants, intact roots, 27 °C, or *H_Intact_27*) reduced colonisation, yielding a gradient from highly susceptible (*M_Cut_32*) to tolerant plants without symptoms that could not be analysed (*H_Intact_27*).

Bottleneck stringency depends primarily on root integrity. Across conditions, the dominant determinant of entry diversity was root state: intact roots admitted low diversity, cut roots admitted high diversity (Fig. 5b). We summarised bottleneck stringency by a parameter θ retrievable from each model ($\theta_{\mathrm{STAMP}} = N_b$; $\theta_{\mathrm{CR}} = \mu_{\mathrm{CR}}/r_{\mathrm{CR}}$; $\theta_{\mathrm{BS}} = v$; $\theta_{\mathrm{IR}} = \mu_{\mathrm{IR}}/r_{\mathrm{IR}}$; Table 1). In time-resolved settings, θ quantifies the rate at which new entry occurs, relative to expansion of established lineages, rendering a "founder-number" definition inappropriate. In the models $\mathcal{M}_{\mathrm{CR}}$ and $\mathcal{M}_{\mathrm{IR}}$, the underlying entry rate μ and population growth rate r can also be deduced from θ.

In $\mathcal{M}_{\mathrm{BS}}$, θ_{BS} represents a relative speed at which the root barrier is traversed by the pathogen, a higher speed leading to a more simultaneous entry of pathogen. Because $\mathcal{M}_{\mathrm{BS}}$ fits best overall (Figs. S6,S6), we used θ_{BS} for comparisons (Fig. 5c). Intact roots showed stringent bottlenecks (median $\theta_{\mathrm{BS}} \approx 1.5$–2), whereas cut roots admitted greater diversity (median $\theta_{\mathrm{BS}} \approx 4$–5). A PERMANOVA test was used to assess the individual contribution of each factor to θ_{BS} (Fig. S7). Only root condition significantly affected θ_{BS} ($R^2 = 16.3\%$) indicating that θ_{BS} neglects susceptibility gradients driven by genotype or temperature. This is expected: θ summarises the endpoint diversity, but not the quantity of pathogens within the plant host.

Growth and entry rates predict susceptibility. Although slightly inferior in overall fit to $\mathcal{M}_{\mathrm{BS}}$, $\mathcal{M}_{\mathrm{IR}}$ has a key advantage: it integrates diversity with CFU and sampling time to estimate the pathogen growth rate r_{IR} (Fig. 5d) and root permeability (entry rate) μ_{IR} (Fig. 5e) for each plant. Both metrics tracked susceptibility more faithfully than θ_{BS}. All three factors (root condition, genotype,

temperature) significantly affected r_{IR} and μ_{IR} (PERMANOVA; Fig. S7). Genotype was the principal driver of growth ($R^2 = 64.6\%$), with a roughly twofold increase of r_{IR} in susceptible plants. Root scarification and elevated temperature contributed additional significant but small effects on r_{IR} ($R^2 =$ 3.0% and 3.2%, respectively). For permeability, root scarification was dominant ($R^2 = 24.4\%$), with significant contributions from genotype and temperature ($R^2 = 5.1\%$ and 2.6%).

Diversity profiles alone are insufficient to characterise time-resolved bottlenecks. Because motility and growth affect both establishment of diversity and *in planta* load, diversity must be interpreted jointly with CFU and time. The couple $(r_{\mathrm{IR}}, \mu_{\mathrm{IR}})$—rather than a single bottleneck metric—captures the dynamics that distinguish susceptibility from tolerance. The ratio $\theta_{\mathrm{IR}} = \mu_{\mathrm{IR}}/r_{\mathrm{IR}}$ can be estimated from diversity alone but remains non-explanatory to describe susceptibility driven by an increase in both permeability μ_{IR} and growth rate r_{IR}.

The role of plant size was also investigated by integrating root samples weight as a proxy for a *plant size* factor (PERMANOVA; Fig. S7). An important contribution of plant size to r_{IR} ($R^2 = 37.3\%$) was mostly drawn from the genotype factor because tolerant plants were typically bigger than susceptible plants in our setup. When integrating contribution of plant size to μ_{IR}, only plant size, root condition and genotype were significant (respectively $R^2 = 4.7\%$, 25.0%, and $1, 2\%$), indicating that bigger plants are typically more susceptible on both $(r_{\mathrm{IR}}, \mu_{\mathrm{IR}})$ regardless of other factors.

1.5 Time-resolved bottleneck models apply to animal infections

To test generality of our approach beyond plants, we applied our model-testing framework to a published dataset of *Pseudomonas aeruginosa* bacteraemia in mice (Fig. 2C in reference[5]), previously reanalysed with STAMPR (Fig. 4 in reference[2]). Following intravenous inoculation of tagged *P. aeruginosa*, organ-specific bottlenecks estimated by N_b and N_r were reported (Fig. 6a;[2,5]). Tag-relatedness analyses indicated that lung, spleen, and liver are seeded from blood-circulating bacteria, whereas gallbladder and the gastrointestinal tract derive from mixtures of liver-seeded and blood-circulating populations[2,5].

The original studies already disfavour an instantaneous bottleneck: observations that N_b is consistently underestimated when compared to N_r was interpreted as evidence of clonal expansion during organ colonisation[2]. We concur that systemic infection reflects two concurrent processes: entry of circulating bacteria into organs (an entry rate μ) and within-organ proliferation (a growth rate r). Our framework addresses two questions left open by the STAMP(-R) metrics: (*i*) what is the nature of the bottlenecks, and (*ii*) why do founder-number estimates fail to capture the dynamics?

Model comparison identifies time-resolved bottlenecks. Error-curve comparisons show that an instantaneous model ($\mathcal{M}_{\mathrm{STAMP}}$) poorly fits organ diversity profiles, whereas time-resolved models fit substantially better (Fig. 6b; Fig. S8). From the best-fitting model ($\mathcal{M}_{\mathrm{IR}}$), we extract θ_{IR}, an interpretable bottleneck stringency index (Fig. 6c). Unlike founder counts, θ_{IR} reflects whether colonisation proceeds in a monoclonal or diversified mode under continuous entry.

Entry and growth rates resolve organ-specific dynamics. Because our approach integrates diversity with CFU and sampling time, we can estimate organ-specific entry μ_{IR} and growth r_{IR}. Entry rates (Fig. 6d) indicate that lung, spleen, and liver are relatively permeable to circulating bacteria, whereas gallbladder and the gastrointestinal tract are comparatively impermeable—consistent with diversified colonisation in the former and monoclonal expansions in the latter. These conclusions agree with relatedness-based inferences that the gastrointestinal tract is not directly seeded from blood[2,5], while adding a quantitative flow-rate perspective via μ_{IR}. Estimated growth rates (Fig. 6e) further reveal that lung and spleen share similar dynamics ($r_{\mathrm{IR}} \approx 0.3\ \mathrm{h}^{-1}$), whereas liver, gallbladder, and most of the gastrointestinal tract (except stomach) exhibit roughly twofold higher apparent growth.

Revisiting the "liver filter" interpretation in the *P. aeruginosa* infection. A prior interpretation suggested that the liver acts as a filter for bacteria prior to their entry into the gallbladder, as evidenced by reduction in N_b (or N_r) from liver to gallbladder[2,5]. Our time-resolved analysis refines this view: organ permeability to entry indeed decreases between liver and gallbladder, and growth markedly increases downstream. Elevated growth amplifies competitive exclusion, reducing effective diversity and creating an apparent bottleneck even under ongoing entry. Notably, recent work links high replication potential of *P. aeruginosa* to stringent gastrointestinal tract bottlenecks[14], consistent with our growth-driven explanation.

Model-based metrics outperform STAMPR in biological meaning and statistical power. We reanalysed a second dataset of systemic bacteraemia by *Klebsiella pneumoniae* following a pneumonia in mice (Fig. 1 in reference[13]). Again, time-resolved models better fitted organ diversity compared to $\mathcal{M}_{\mathrm{STAMP}}$ in that dataset (Fig. S9). To further showcase the performances of our approach, we compared the improvements of our model-based metrics over the full extend of available STAMPR metrics deployed to describe the infection dynamics (Fig. S9).

As a short summary: an appropriate index θ_{IR} replaced N_s as a bottleneck effects estimator avoiding the confusion of time-resolved or instantaneous bottleneck and being more statistically discriminant on Cohen's D effect size; the estimated growth rate r_{IR} provided a biological meaning to difficultly interpretable empirical estimators of bacterial expansion CFU/N_s and N_s/N_b; μ_{IR} provided an overlooked estimator for pathogen transfer rate, inaccessible in STAMPR. In term of performances, the model-based metrics required no logarithmic transformations for parametric tests and appeared to harbour improved effect size, indicating they tend to be more robust and more discriminative when compared to their STAMPR counterpart.

***K. pneumoniae* mode of dissemination is observable on growth at a host level.** The authors of reference[13] characterised two disseminations patterns of *K. pneumoniae* from the lung to systemic sites: *metastatic dissemination* when the infection originated from a few dominant that first expanded in the lung, or *direct dissemination* when diversified multiclonal pathogen populations spread to the organs.

To consolidate this conclusion, we investigated r_{IR} across multiple organs which is not possible using only CFU. The apparent pathogen growth was surprisingly similar across the different organs with a typical $r_{\mathrm{IR}} \approx 0.45\mathrm{h}^{-1}$ in *direct disseminations* at 24h post-infection (Fig. S9). In contrast, *metastatic disseminations* showed a generalised 40% increase in r_{IR} across all organs. This indicates that *metastatic dissemination* is not only produced by increased replication at the lung as originally concluded by the authors but rather appears to be characterised by a host-wide increase in pathogen replication.

2 Discussion

Our approach improves tools for analysing neutral barcoding experiments by treating diversity profiles structure as mechanistic readouts rather than reducing them to founder-based metrics (N_b, N_r, N_s). Founder-based metrics are attractive for their simplicity, yet they implicitly assume that entry and growth are decoupled during a bottleneck. A common practice has been to interpret high values of N_s/N_b or N_r/N_b from STAMPR as evidence of clonal expansion during colonisation[2,12,13,17]. This logic, while useful, underscores the inadequacy of founder-based metrics for systems where growth and entry co-occur.

Time-resolved mechanistic models have been proposed previously—notably RESTAMP for *Vibrio cholerae* in the mouse gastrointestinal tract[3,8]—emphasising transfer rates and growth across compartments. Potential concerns arise for RESTAMP: its parameter complexity (e.g., ~ 30 fitted parameters[8]), its reliance on N_b to infer secondary parameters and additional conceptual assumptions that neglects migration effects in infectious context[3]. Since N_b ignores temporal or spatial colonisation dynamics, secondary parameters may overfit and lose biological relevance unless directly validated against tags frequency data. Instead, we tested a panel of mechanistic models and selected the one best supported by the actual data. This presents three advantages. First, model assumptions need not be verified *a priori*: poor models are rejected by comparative fit. Second, the nature of the bottleneck (instantaneous *vs.* time-resolved) emerges from model performance. Third, unlike empirical corrections (*e.g.*, STAMPR), all tested models are mechanistic, with parameters that have explicit biological interpretations[29].

A counter-intuitive property of bottleneck metrics θ (*i.e.*, N_b, N_r, N_s, θ_{CR}, θ_{BS}, θ_{IR}) is that they do not quantify host defences or susceptibility under time-resolved dynamics. Conceptually, θ summarises the *established* diversity profile but does not reveal how many bacteria effectively generated that profile. The latter information requires integrating CFU and time via the entry and growth parameters μ and r. In practice, questions about barrier function and susceptibility are related to *amounts* of pathogen, not just diversity. Improved host defence (less colonisation) manifests in μ and r, but not necessarily in θ. This distinction is evident in our data. For example, the *M_Intact_32* condition exhibited fast entry, fast growth and rapid symptoms onset, whereas *H_Intact_32* showed slow entry, slow growth and slow symptoms onset. Both yielded similar θ_{BS} and θ_{IR} values, yet they represent different susceptibility

states because $(\mu_{\mathrm{IR}}, r_{\mathrm{IR}})$ differ. This misconception of θ traces back to the STAMP model: N_b conflates diversity profile structure (θ) with entry rate (μ) under an instantaneous assumption. In a time-resolved system, N_b-derived indicators neglect the entry component μ. Because N_b-derived indicators or θ_{BS} do not give access to μ and r, it would be ill-advised to use them to estimate host defences parameters without associating an estimation of (μ, r) using $\mathcal{M}_{\mathrm{CR}}$ or $\mathcal{M}_{\mathrm{IR}}$.

One additional precaution of time-resolved dynamics is that the estimation of (μ, r) depends on the time of sampling. As growth can only be estimated during exponential phase, absolute estimations of (μ, r) are only true if CFU are also measured during exponential phase. Since diversity profile (θ) itself is robust to time of sampling, apparent estimations of (μ, r) should still remain accurate at saturation of CFU but only for relative comparisons rather than absolute quantification. A major advantage of controlling time of sampling is the ability to provide an accurate estimation of r per individual plants and with a single sampling time (Fig. 5e) while also remaining coherent with classic linear regression on CFU over time (Fig. 1b).

We questioned the relation between spatial structure and intrinsic fitness variation. Throughout this study, we assume *fitness neutrality*: all tagged lineages share the same fitness. We also assume spatial and temporal homogeneity, because even without genetic drift, heterogeneity can generate unequal tag frequencies by altering arrival times, local densities, or local growth conditions. For example, outputs of $\mathcal{M}_{\mathrm{CR}}$ can resemble an instantaneous-entry scenario with differentially growing subpopulations; in such cases, the apparent differences in growth could arise from micro-environmental conditions. In $\mathcal{M}_{\mathrm{CR}}$ and $\mathcal{M}_{\mathrm{IR}}$, when heterogeneity is pronounced, μ and r should therefore be interpreted as effective, sample-scale parameters that integrate spatial and temporal effects; recovering "pure" permeability and growth would require spatially resolved measurements and an explicit spatial model. The Bolthausen-Sznitman model $\mathcal{M}_{\mathrm{BS}}$ partially relaxes this limitation by allowing highly skewed offspring distributions characteristic of range expansions. It captures gene-surfing and dead-end events—*i.e.*, consequences of spatial structure—without invoking intrinsic fitness differences[30]; part of this structure is captured by θ_{BS}.

More generally, the host spatial structure may prove to be an important factor to decipher pathogen infection dynamics. Because space seems to be limiting for the pathogen in the studied contexts, our impression is that key steps of the infection can favour selective pressure on high motility instead of high growth for the pathogen. Evidences can be seen in *P. aeruginosa* infections, where the maximum of dissemination of *P. aeruginosa* is observed in blood-connected organs but the maximum of growth is observed in the gastrointestinal tract. Given this pattern, our hypothesis is that there is beneficial outcome for the pathogen to quickly colonise the gastrointestinal tract, either because it is the place that maximises transmission and survival of the pathogen line through the faeces or as a potential niche for chronic infection.

Focusing on *R. pseudosolanacearum* infection in plants, two quantitative mechanisms were investigated to explain the higher tolerance of Hawaii7996 relative to Marmande tomato plants: reduced within-plant growth of the pathogen was consistent with prior work[18] although quantitative differences

in root permeability were unclear. Root scarification increased permeability at the root surface and, unexpectedly, also increased within-plant growth, suggesting that scarification compromises internal root defences. Root barrier components are important in controlling plant compounds and the root-associated microbiome[31,32,33]. Our hypothesis is that scarification allows leakage of high quantity of plant exudates such as glutamine, which is both a chemoattractant for soil bacteria[34] and a preferential substrate for *R. pseudosolanacearum* growth during infection[35]. Similarly, killing of cortical cells[19,20,21] could explain the increasing permeability described over the course of infection. Widening of a breach in the xylem would increase spatial access for the pathogen but could also provoke increasing leakage of the aforementioned plant exudates, accelerating attraction of pathogen to the wound. High temperature further promoted susceptibility, increasing both growth and permeability. For *R. pseudosolanacearum* infection dynamics, our data support growth as the primary driver of susceptibility, with permeability as a secondary contributor. The effects of growth (r_{IR}) and permeability (μ_{IR}) are not equivalent: entry alone cannot account for the bacterial loads observed at sampling. A minimum growth rate is required for detectable colonisation, whereas detectable entry can occur without colonisation. This is evident in non-symptomatic tolerant plants (Fig. S2), where trace amounts of *R. pseudosolanacearum* were detected but did not progress to colonisation. Permeability remains important, particularly as an accelerator of early infection. Across sampled plants, r_{IR} and μ_{IR} were positively correlated (Spearman rank correlation $R^2 = 0.40$, $p < 0.05$; Fig. S7): plants permissive to entry also tended to support faster growth, indicating partial coupling rather than complete independence of these processes.

How common are instantaneous versus time-resolved bottlenecks? The field increasingly recognises the need to account for time in neutral barcoding studies[2,8]. While direct evidence for truly instantaneous events remains scarce, signatures consistent with time-resolved dynamics are widespread: heterogeneous tag frequencies within samples, systematic declines in N_b across space or time, $N_r/N_b > 1$ or presence of numerous low-frequency tags. Such patterns likely arise when within host dissemination and growth are intertwined. On this basis, several studies may have applied instantaneous-bottleneck analyses to systems where time-dependent effects actually dominate.

Because the advantages of a model testing approach exceeds those of N_b-derived indicators in error assessment, relevance of the used metrics and inference on the infection dynamics, we advocate for a global reanalysis of STAMP(-R) articles under a time-resolved model approach. We foresee that unappreciated biological results may be uncovered in the following cases: (*i*) studies that used only N_b and may have overlooked major aspects of the infection dynamics[1,4,5,6,7], (*ii*) studies of colonisation across continuous space (*e.g.* gastrointestinal tract colonisation) that neglected contributions of migration and growth effects by using N_b-derived indicators[2,8,11,12,13,14,15,16], (*iii*) studies that empirically uncovered the importance of time dimensions using N_b-derived indicators but were limited in their analysis[11,12,17], (*iv*) studies that directly addressed relations between CFU dose effects and bottleneck using N_b-derived indicators but did not pair the two in an appropriate model[9,10,11].

The notebook used in the study is made available along with all analyses and reanalyses performed

in the study. Application of the approach should be straightforward with minimal knowledge in R and Python, and on any neutral barcoding dataset, as long as sample names, experimental conditions, tag frequencies, bacterial load, time of sampling and corresponding inocula are fully explicit.

3 Figures

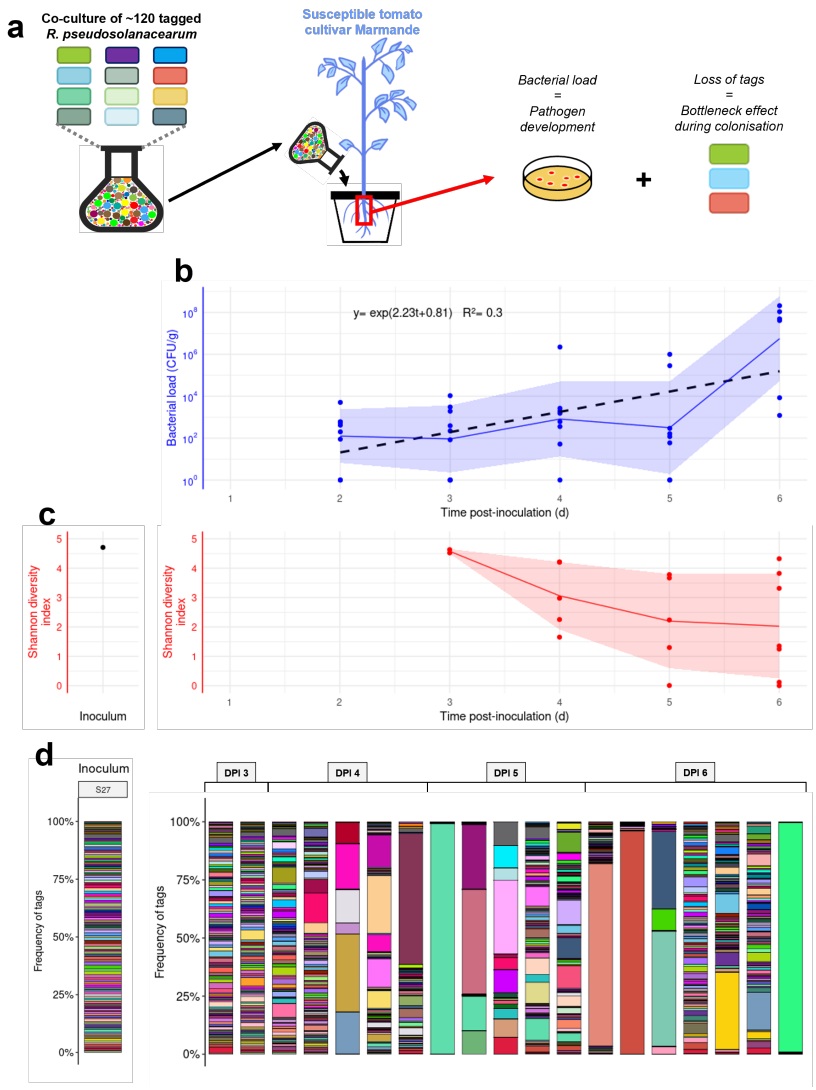

Figure 1: Roots of susceptible tomato (cv. Marmande) are infected by limited quantities of individual *R. pseudosolanacearum* cells. **a.** Schematic overview of a STAMP experiment. A collection of ~ 120 isogenic strains was produced by inserting a neutral 20 bp polymorphism region in the chromosome of *R. pseudosolanacearum* strain GMI1000 (the STAMP tag). Co-cultures of 119 tagged strains were used to infect Marmande tomato plants by soil-drenching. Plant roots are collected to evaluate the establishing pathogen population. Two paired informations can be extracted from a STAMP analysis. First, the bacterial load, indicative of the colonisation. Second, as the tagged strains are constructed to have identical fitness, a loss of artificial diversity is indicative of bottlenecks (*i.e.* population-limiting effects). **b.** Kinetics of bacterial load between 2 and 6 DPI in the collected root samples (log scale). Each day, $n = 8$ or $n = 9$ plants were sampled. The local average value (blue line) and the local standard deviation (blue area) are represented. The black dotted line and the corresponding equation represents the fit of a linear regression of the form $y = e^{a\,t+b}$. **c.** Shannon diversity index calculated for the colonising population between 3 and 6 DPI in the roots. The local average value (red line) and the local standard deviation (red area) are represented. Sufficient bacterial load for sequencing diversity was obtained in root at 3 DPI or later (typically above $\sim 10^4$ CFU/g). A reference diversity value of 4.71 was calculated in the inoculum. All diversity values in roots are lower than this reference. **d.** Diversity profiles for each individual sample and the inoculum. Each colour represents the relative frequency of a unique tag among the 119 used tag. The profiles are grouped by day of sampling (top row).

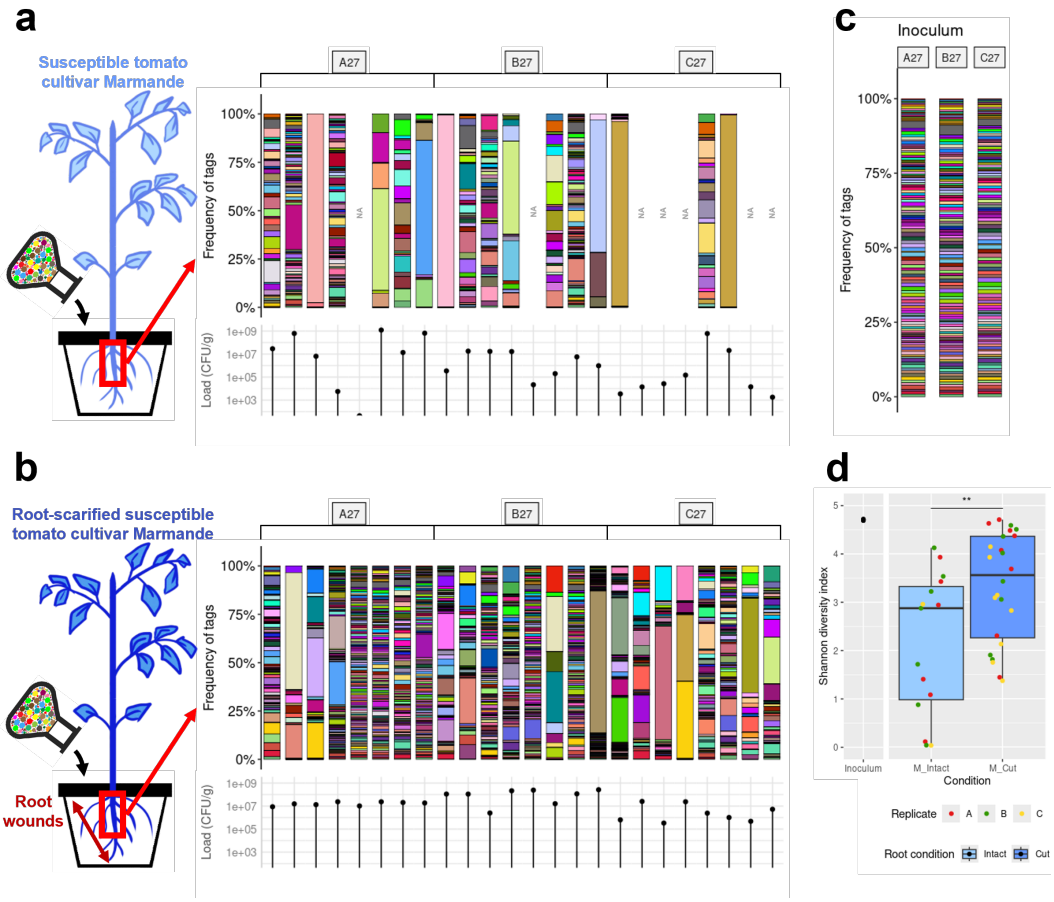

Figure 2: The root-entry bottleneck depends on the physical integrity of the roots. **a and b.** Diversity profiles during colonisation of the roots of control intact Marmande tomato plants (panel **a**, $n = 24$) or root-scarified Marmande tomato plants (panel **b**, $n = 24$). Each colour represents the relative frequency of a unique tag among the 119 from the inoculum. For each sample, bacterial load is provided as a barplot under the diversity profiles (logarithmic scale). A blank space with "NA" is presented when sequencing was unsuccessful due to low bacterial load. **c.** Diversity profiles in the inocula "A27", "B27" and "C27" corresponding to the three time-independent replicates of infection in panel a and b. **d.** Shannon diversity index calculated in the roots of control intact Marmande tomato plants (*M_Intact*) or cut Marmande plants (*M_Cut*). Statistical test: Wilcoxon-Mann-Whitney test (two sided, **: $p = 0.0094$). Reference values were calculated for the three inocula (range between 4.70 to 4.72). Diversity values in root samples were systematically lower than in their corresponding inoculum.

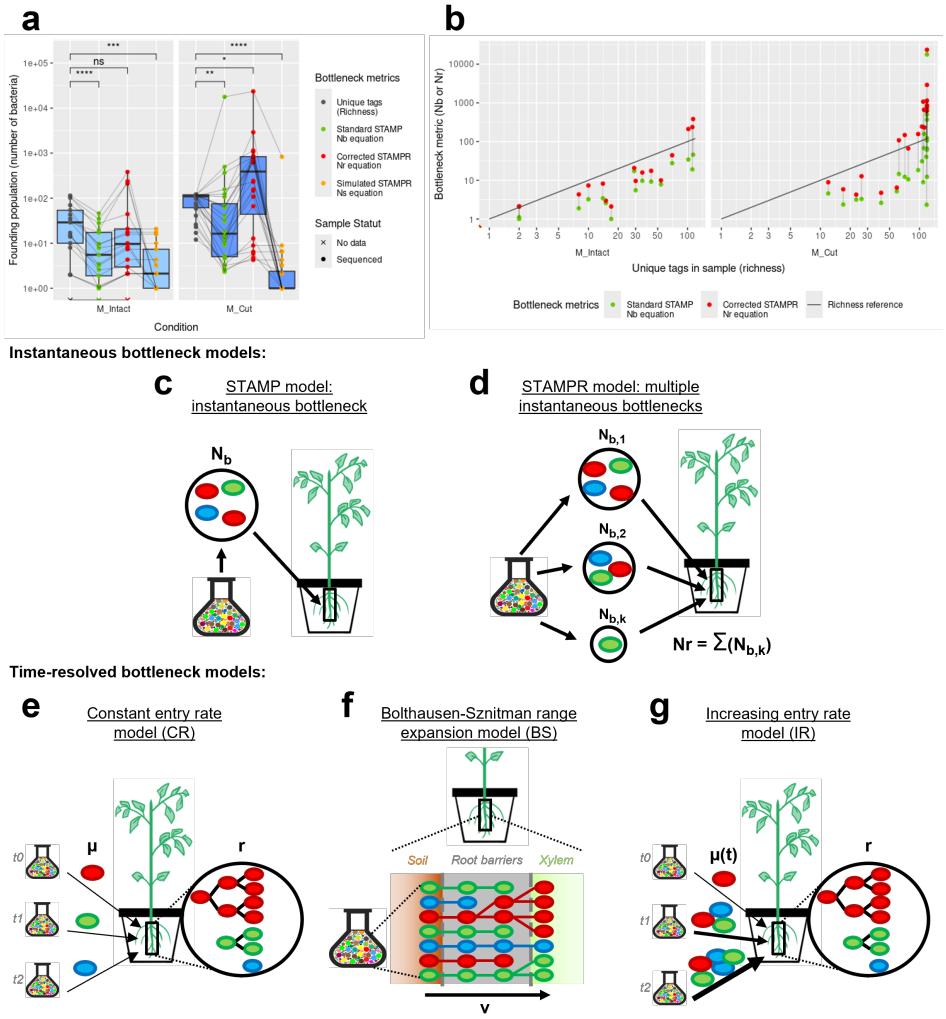

Figure 3: Diversity profiles in the pathogen populations better support "time-resolved" rather than "instantaneous" bottleneck models. **a.** Bottleneck in intact (*M_Intact*) or root-cut Marmande tomato plants (*M_Cut*) according to the metrics of richness, N_b [1] or respectively N_r and N_s [2] (logarithmic scale). A line connects the different metrics calculated in the same sample. Statistical test: Wilcoxon signed-rank test (two-sided, ns: $p > 0.05$; *: $p < 0.05$; ** $p < 0.01$; ****: $p < 0.0001$). **b.** N_b and N_r in sample as a function of richness (log-log scale). A reference line $y = x$ represents richness, N_b or N_r under the line are lower than richness in the same sample. A line connects N_b and N_r calculated from the same sample. **c.** "Instantaneous bottleneck" or "STAMP" model underlying the N_b metric [1]. A bottleneck event is simplified to a unique, quasi-instantaneous entry of N_b bacteria in the plants. The N_b founder cells are those that successfully overcame host defences. In a second step, the founders grow homogeneously into the observed pathogen population. **d.** "Multiple instantaneous bottlenecks" or "STAMPR" model empirically interpreted from the algorithms of the N_r and N_s metrics [2]. Plant colonisation is supposed to occur according to k events of instantaneous entry, each contributing to $N_{b,k}$ new founders. Each k subpopulation represents a different proportion of the total population. The assumptions of instantaneous entry are inherited from the STAMP model. **e.** "Constant entry rate" or CR model. Plant colonisation is supposed to be a combination of a constant entry process and a pure growth process. Pathogens enter the roots at a constant entry rate (or permeability) μ_{CR}. Simultaneously, already present pathogens grow at an exponential rate r_{CR}. In analogy to N_b, the bottleneck metric in the CR model is the ratio between entry of pathogen and occupation of space by growth $\theta_{\mathrm{CR}} = \mu_{\mathrm{CR}}/r_{\mathrm{CR}}$ and informs on the quantity of unique cells that can enter the plant before saturation. A low θ_{CR} indicates a colonisation that is mostly governed by growth (a stringent bottleneck). **f.** "Bolthausen-Sznitman" or BS model. The crossing of the root barriers is modelled by a range expansion in a finite population [25,30]. Pathogen cells migrate randomly within the barrier and divide at a density-dependent rate (cells in more crowded areas divide less often). The cells that manage to cross the barrier then colonise the plant. The resulting sampling of tags can be obtained using the Bolthausen-Sznitman coalescent, see Section 4.7. In analogy to N_b, the bottleneck metric $\theta_{\mathrm{BS}} = v$ is the relative speed at which pathogens can cross the root barriers and reach the final compartment. A low value indicates a slow breaching of the roots barriers allowing for more branching of pathogen cells lines thus a more stringent bottleneck. **g.** 'Increasing entry rate" or IR model, a generalisation of the CR model. Here the colonisation of the plant is a combination of an exponentially increasing entry process and a pure growth process. As entry increases over time, an entry rate factor (or permeability factor) μ_{IR} governs the acceleration of entry of pathogen over time. Simultaneously, already present pathogens grow at an exponential rate r_{IR}. Similarly to the CR model, a low bottleneck metric $\theta_{\mathrm{IR}} = \mu_{\mathrm{IR}}/r_{\mathrm{IR}}$ represents a stringent bottleneck.

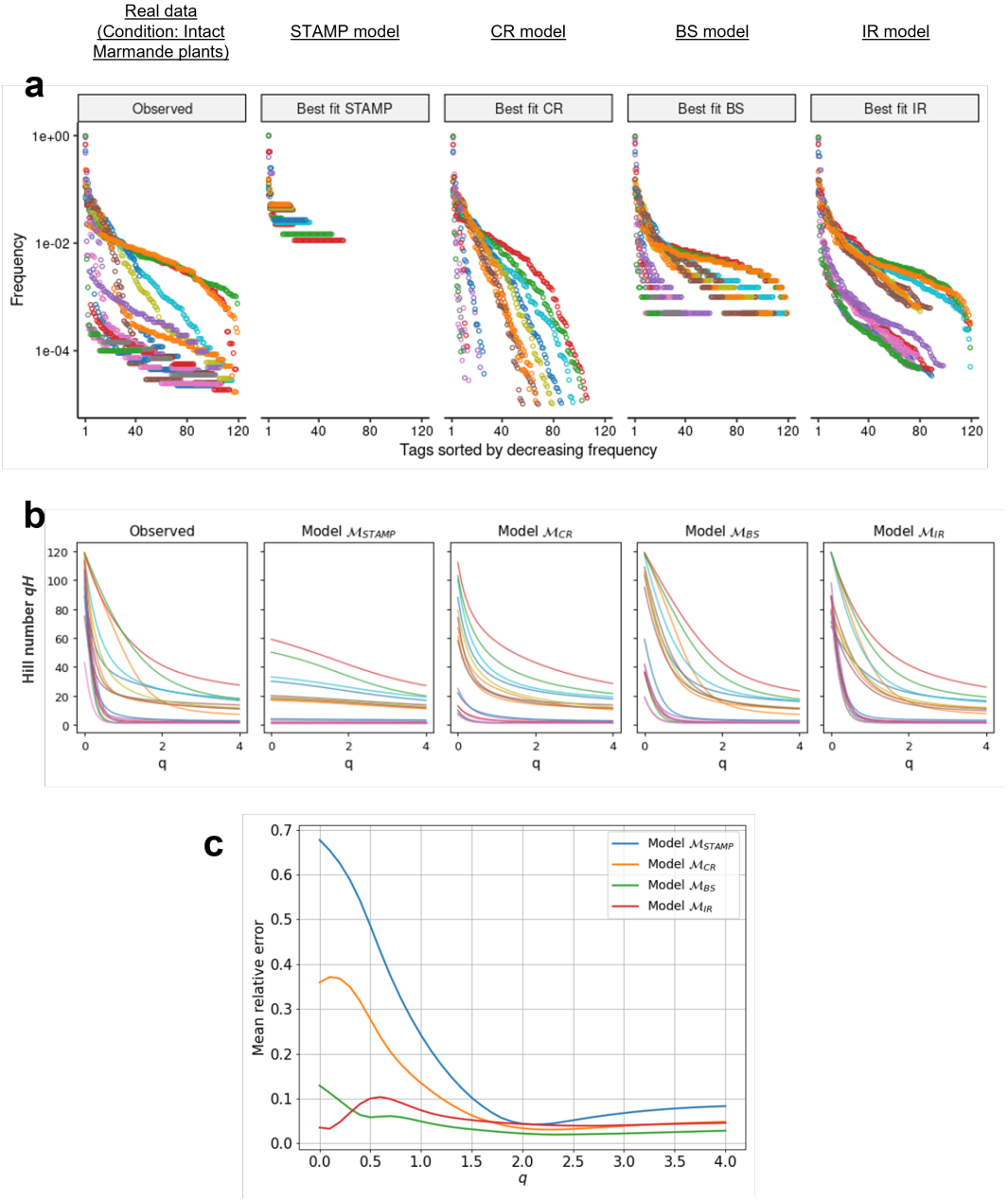

Figure 4: A time-resolved bottleneck is the most probable mode of colonisation of plant roots. **a.** Diversity profiles observed in samples (intact Marmande tomato plants) compared to the corresponding best fitting profiles under simulation of the models $\mathcal{M}_{\mathrm{STAMP}}$, $\mathcal{M}_{\mathrm{CR}}$, $\mathcal{M}_{\mathrm{BS}}$ and $\mathcal{M}_{\mathrm{IR}}$ (logarithmic scale). Each colour represents a unique sample. **b.** Diversity profiles in samples and simulations according to the Hill numbers ${}^{q}H$ from order $q = 0$ (giving more importance to richness) to order $q = 4$ (giving more importance to evenness). For a given order q, a high value ${}^{q}H$ indicates a high diversity. Each colour corresponds to a sample profile from panel a. **c.** Error between the simulations from the four models and the real data in the range from $q = 0$ to $q = 4$, averaged over all infection conditions in Fig. 2 and Fig. 5.

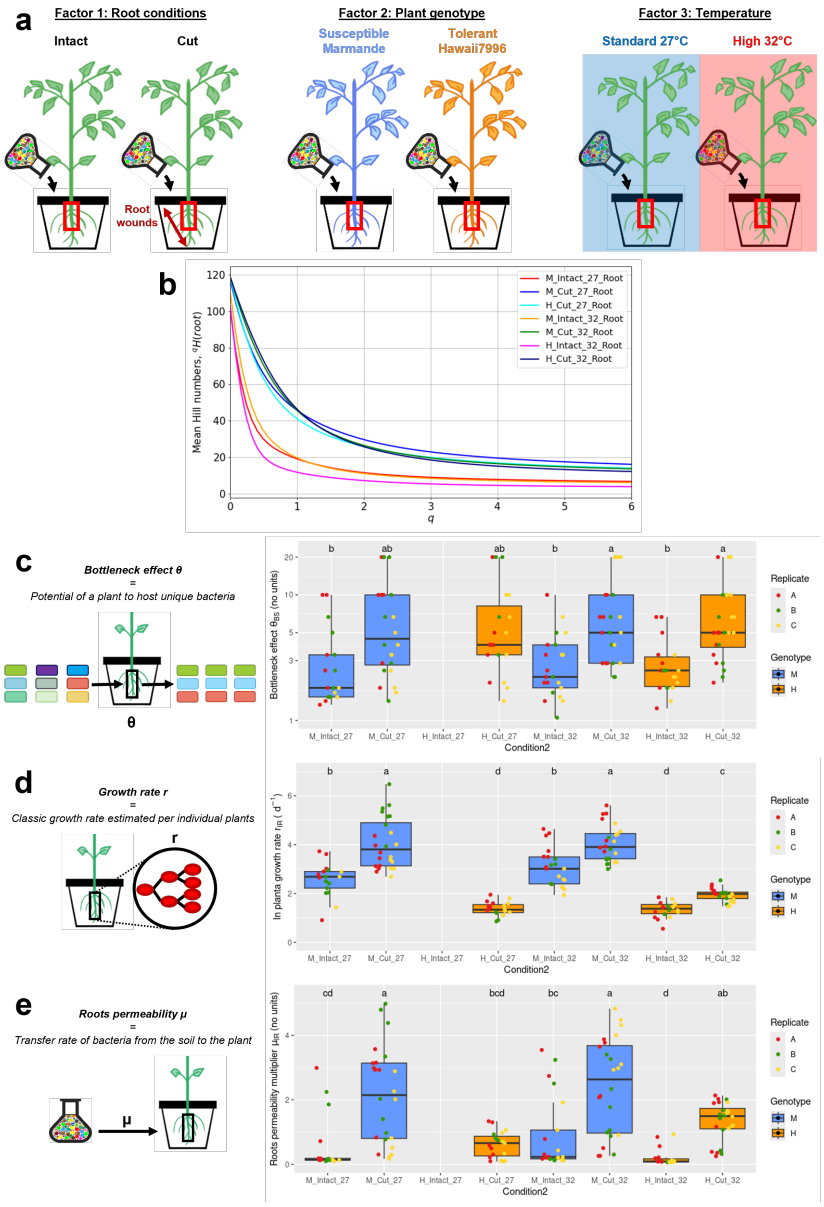

Figure 5: Susceptibility to *R. pseudosolanacearum* can be characterised by time-dependent metrics in a time-resolved bottleneck. **a.** Schematic overview of the experimental infection conditions. Eight conditions of infection were tested on root colonisation by combining three factors affecting plant susceptibility ($n = 24$ infected plants in each condition). A "Root condition" factor tested an artificial lift of root defences with the infection of intact plants versus root-cut plants. A "Plant genotype" factor tested the root defences behaviour in susceptible cultivar Marmande versus tolerant cultivar Hawaii7996. A "Temperature" factor tested the effect of environment on the colonisation with a standard temperature (27°C) versus a high temperature (32°C) during infection. **b.** Hill number curves on the range $q = 0$ to $q = 6$ for the pathogen diversity in each sample averaged over each condition. (Conditions: M: Marmande, H: Hawaii7996, I: Intact, C: Cut). Condition *H_Intact_27* was tolerant and did not yield sufficient colonisation to allow sequencing of the diversity. **c.** Estimated bottleneck parameter $\theta_{\mathrm{BS}} = v$ obtained with $\mathcal{M}_{\mathrm{BS}}$ (logarithm scale). θ_{BS} is a metric of the "bottleneck effect" in a time-resolved bottleneck model *i.e.* an indicator of monoclonal or diverse colonisation. A low value indicates a stringent bottleneck. Statistical test: Kruskal-Wallis test with *post hoc* Fisher's LSD test (CLD threshold: $p < 0.01$). **d.** Growth rate r_{IR} in individual plant roots estimated from the parameter $\theta_{\mathrm{IR}} = \mu_{\mathrm{IR}}/r_{\mathrm{IR}}$ with $\mathcal{M}_{\mathrm{IR}}$. Statistical test: Kruskal-Wallis test with *post hoc* Fisher's LSD test (CLD threshold: $p < 0.01$). **e.** Entry rate (or permeability) multiplier μ_{IR} in each individual plant roots estimated from the parameter $\theta_{\mathrm{IR}} = \mu_{\mathrm{IR}}/r_{\mathrm{IR}}$ with $\mathcal{M}_{\mathrm{IR}}$. The metric μ_{IR} is an indicator of the transfer rate of pathogen from soil to the roots of the plants. A high value indicates faster entry of pathogen over time. Statistical test: Kruskal-Wallis test with *post hoc* Fisher's LSD test (CLD threshold: $p < 0.01$).

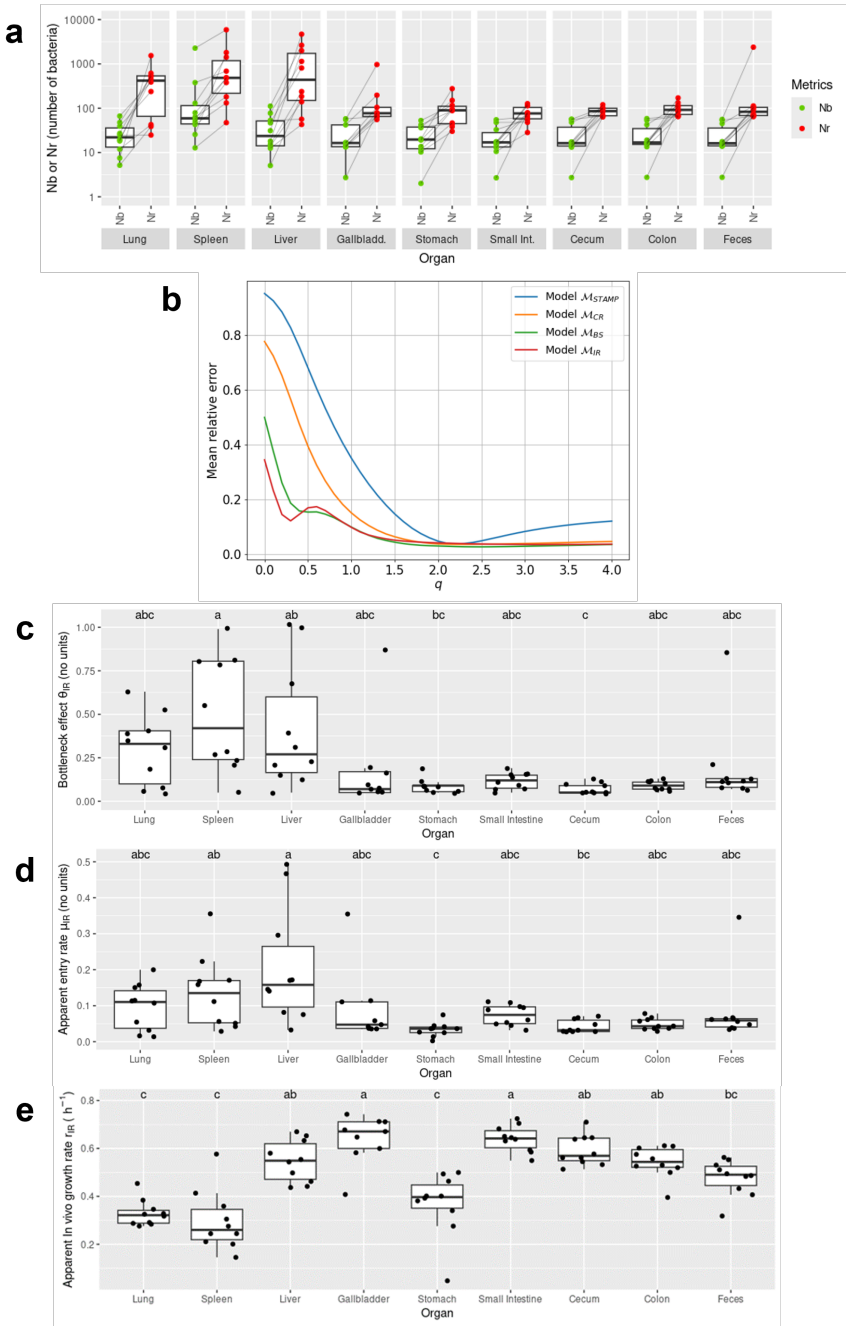

Figure 6: Time-resolved bottleneck models provides insights on overlooked systemic infection of *Pseudomonas aeruginosa* in mouse (original data from Fig. 2C of article[5], $n = 10$ mice). **a.** Recalculation of the two bottleneck metrics N_b and N_r used during prior analyses of the dataset[2,5] (logarithmic scale). A line connects the two metrics calculated on the same sample. **b.** Error between the simulations from the four models and the *P. aeruginosa* diversity data in the range from $q = 0$ to $q = 4$ (averaged over all infection conditions). **c.** Estimated bottleneck parameter θ_{IR} obtained with $\mathcal{M}_{\text{IR}}$ (logarithmic scale). A low value indicates a stringent bottleneck. Statistical test: Kruskal-Wallis test with *post hoc* Fisher's LSD test (CLD threshold: $p < 0.01$). **d.** Apparent growth rate r_{IR} in each individual plant roots estimated from the parameter $\theta_{\text{IR}} = \mu_{\text{IR}}/r_{\text{IR}}$. Whether r_{IR} corresponds to the actual growth rate *in vivo* depends on the assumption that samples were collected during exponential growth of the pathogen. Statistical test: Kruskal-Wallis test with *post hoc* Fisher's LSD test (CLD threshold: $p < 0.01$). **e.** Apparent entry rate multiplier μ_{IR} of pathogens in each organ and estimated from the parameter $\theta_{\text{IR}} = \mu_{\text{IR}}/r_{\text{IR}}$. In this context, μ_{IR} represents the contribution of systemic circulating bacteria to the colonisation of an organ. The accuracy of this estimation is conditioned to the accuracy of r_{IR}. A high value indicates faster entry of pathogen over time. Statistical test: Kruskal-Wallis test with *post hoc* Fisher's LSD test (CLD threshold: $p < 0.01$).

4 Online methods

4.1 Construction of the STAMP collection in *R. pseudosolanacearum* and co-culture of the strains

123 oligonucleotides of a 20 bp random sequence (referred as "tag", list in supplementary document "STAMP123_tags.fasta") were synthesised and hybridised with their complementary sequence to form inserts with cohesive extremities BsrGI and BglII. These fragments were inserted by restriction–ligation (BsrGI / BglII) in a pRCT-GWY[22] derived plasmid denoted pNP413. The tag is contained inside a genetic cassette of 6 kb containing a *tetR* gene, a *mCherry* gene and two flanking regions of 1 kb used for homologous recombination with *R. pseudosolanacearum* strain GMI1000 in the chromosome[22].

Produced plasmids were chemically transformed into calcium-competent *E. coli* strain DH5alpha and selected using LB medium + tetracycline 10 mg/L. Clones were verified using a wild-type discriminating PCR and Sanger sequencing of the STAMP tag (Eurofins). Validated plasmids were purified in 50 μL ultrapure water using 2 mL of stationary-phase culture with a column extraction kit (BS614, Bio Basic). 10 μL of plasmid was linearised using SfiI enzyme and mixed with 200 μL of *R. pseudosolanacearum* strain GMI1000 from a liquid culture in exponential phase, grown 1 week at 28 °C in MP medium + 2% glycerol. The mix was deposited on MP medium + 2% glycerol Petri dishes and incubated 2 days at 28 °C for natural transformation. Three days later, the bacterial lawn was suspended in distilled water and isolated on Phi medium + tetracycline 10 mg/L Petri dishes. The obtained *R. pseudosolanacearum* strains were validated for the correct insertion of the 6 kb cassette using a wild-type discriminating PCR and Sanger sequencing of the STAMP tag (Eurofins).

Individual clones were grown in 96-well microplates at 28 °C in 250 μL of Phi medium + tetracycline 10 mg/L in an Omega FLUOstar spectrophotometer (BMG Labtech) until stationary phase. An OD_{600nm}-adjusted volume (50 $\mathrm{AU_{OD}} * \mu$L per well) was used to inoculate a secondary microplate culture in the same conditions. At stationary phase, wells were pooled 8-by-8 using OD_{600nm}-adjusted volumes (100 $\mathrm{AU_{OD}} * \mu$L per well) for inoculation of tertiary Erlenmeyer cultures at 28 °C in 20 mL Phi medium + tetracycline 10 mg/L overnight. At stationary phase, the OD_{600nm}-adjusted volumes of each 8-tag pool (1400 $\mathrm{AU_{OD}} * mL$) were mixed with 500 μL glycerol 60% for storage at −70 °C. The day before infection, an inoculum of 120 tags was produced by thawing the 15 tubes of 8 tags (total volume $\sim$ 25 mL) and growing them directly in an Erlenmeyer with 250 mL of Phi medium + tetracycline 10 mg/L at 28 °C overnight. Upon validation of these final co-cultures, one tag (tag007) was found missing but an otherwise almost perfect stoichiometry was obtained for the 119 other tags. The three remaining tags (denoted tag121, tag122 and tag123) were grown and kept separately for sequencing calibrations.

Used media. LB medium: Yeast extract (Duchefa Biochimie) 5 g/L; Bacto tryptone (Becton Dickinson Difco) 10 g/L; NaCl 10 g/L in distilled water. Phi medium: Bacto peptone (Gibco) 10 g/L; Casamino acid (MP) 1 g/L; Yeast extract (Duchefa Biochimie) 1 g/L in distilled water. MP medium: KH2PO4 3.4 g/L; (NH4)2, SO4 0.5 g/L; MgSO4 (7H2O) 50 mg/L; FeSO4 (7H2O) 125 µg/L in distilled

water. Adjust pH to 7.0 with KOH 10N.

4.2 Plant culture, plant infection and samples collection

For all experiments, tomato plants (susceptible cultivar Marmande "M" or tolerant cultivar Hawaii7996 "H") were sowed in peat-based substrate and then cultivated in 6×6 cm pots until an age of approximately 3 weeks in a phytotron (25.5±1 °C day 12 h / 24±1 °C night 12 h, hygrometry 60±15%). The plants were then acclimated to the final culture chamber for 2 or 3 days either at a standard temperature (27±0.5 °C day 12 h / 26±0.5 °C night 12 h, hygrometry 60±5%) or at a high temperature (32±1 °C day and night 12 h/12 h, hygrometry 70±5%). The days of infection, two technical replicates of 2 mL of the inoculum STAMP co-culture were taken for sequencing of the initial population. The co-culture was diluted using tap water (to an $OD_{600nm} = 0.05$) and 50 mL of diluted co-culture ($\sim 2.5 \times 10^9$ CFU) was used to infect plants by watering. Right before inoculation, the condition of "Root cut" plants was produced by scarifying roots of the plants using a scalpel by drawing an "L"-shaped trench in the pot. "Intact" plants were otherwise watered without scarification.

For the experiments of kinetics of infection, one infection was performed (inoculum S27) on $n = 42$ plants (Conditions M_Intact_27). $n = 8$ or $n = 9$ plants were then sampled between DPI 2 to DPI 6. The plant was unrooted and dirt removed. A root sample was collected corresponding to the whole taproot cut at the highest lateral root and removed from all lateral roots. Samples were weighed, surface-sterilised using 70% ethanol and cleaned using sterile distilled water. Samples were cut into the smallest possible pieces using a scalpel and macerated in 2.5 mL sterile distilled water for approximately 3 h. The macerate was used to determine bacterial load by plating serial dilutions on Phi medium + tetracycline 10 mg/L Petri dishes using an automatic spreader (EasySpiral Pro, Interscience). The remaining $\sim$ 2 mL of macerate was centrifuged and gDNA was extracted from the bacterial pellets using a lysis–isopropanol–ethanol protocol (Wizard Genomic DNA Purification Kit A1125, Promega) in 50 μL final of ultrapure water.

For the experiments with single-point sampling, six temporally independent infections were performed (inocula denoted A27, B27, C27, A32, B32, C32) combining a total of 192 plants (Conditions: M_Intact_27, M_Cut_27, H_Intact_27, H_Cut_27, M_Intact_32, M_Cut_32, H_Intact_32, H_Cut_32). For each condition three replicates were performed $n = 3 \times 8 = 24$. At the first symptoms of wilting (or at DPI 13 or 14 if no symptoms) within a batch of 8 plants in a replicate, the whole batch was collected. Bacterial load was quantified and DNA was extracted for sequencing as described above.

4.3 Library preparation and sequencing of the diversity profiles

For each purified gDNA, absorbance was measured for an $A_{260/280}$ quality ratio. Whenever possible, samples were diluted to an empiric concentration between $[C] = 20$ to 100 ng/μL (corresponding to a theoretical number of unique molecules of gDNA of 3×10^6 to 1.5×10^7 tags/μL) satisfying a non-limiting amount of targets and an accurate measure of concentration. For samples in which

concentration was below 20 ng/μL or gave aberrant values in view of bacterial load (*e.g.* vegetal phenolic compounds), a value N_{max} defined as the *theoretical maximum number of tags* was derived from bacterial load. A 35-cycle adapter PCR1 was performed to amplify a 174 bp region containing the tag. This PCR was performed using primers with the advised 22 bp Nanopore adapter regions for PCR barcoding (SQK-LSK114, Oxford Nanopore Technologies). Additional 4 bp regions were included between primer hybridisation sequence and adapter sequence. These 4 bp represent a "run barcode" that allows filtering of cross-contamination when using the same Nanopore flow cell in several different sequencing runs. For this article, 6 different pairs of primers were sequentially used with different "run barcodes" in this fashion. For samples for which $[C] > 20$ ng/μL and $N_{max} > 2500$ tags/μL, 4 μL of purified DNA was used in a 75 μL PCR1. For samples for which $[C] < 20$ ng/μL and $N_{max} < 2500$ tags/μL or samples that did not amplify in the first condition, a larger volume of 20 μL of purified DNA was used in a 75 μL PCR1 to ensure an adequate number of targets. Samples that did not validate the two first conditions were repurified in the same volume using 2X magnetic bead-based mix in a SPRI protocol[36] before reattempting a PCR1. Samples that were validated for a $\sim$ 226 bp band on gel electrophoresis were then purified using 1.5X magnetic bead-based mix in a SPRI protocol[36] to eliminate primers and to concentrate the PCR product twofold.

2.5 μL of reconcentrated PCR1 product was used in a 30-cycle barcoding PCR2 in a final volume of 25 μL using primers purchased from the Nanopore 96 Barcode Expansion Pack (EXP-PBC096, Oxford Nanopore Technologies). Samples that were validated for a $\sim$ 274 bp band on gel were then quantified for DNA concentration using Quant-iT PicoGreen dsDNA Assay (P7589, Invitrogen) and pooled in equal stoichiometry before a purification with 1.2X magnetic bead-based mix in a SPRI protocol[36]. End-prep and adapter ligation steps were performed according to the PCR barcoding protocol (SQK-LSK114, Oxford Nanopore Technologies) with the exception of SPRI purifications that were adjusted to a 1.5X ratio in accordance with the length of the DNA fragments of interest.

A PromethION flow cell R10.4.1 was loaded with an adjusted quantity of 200 fmol of DNA and data acquisition was performed with a goal of minimum depth of sequencing of $\sim$ 20k unprocessed reads for all samples. The flow cell was washed according to protocol (EXP-WSH004-XL, Oxford Nanopore Technologies) to reuse it for a total of 6 runs of $\sim$ 96 samples. For technical simplicity, some samples went through the whole sequencing process despite not being validated in the early PCR steps. These samples were excluded from the final analysis.

4.4 Raw data processing

DNA sequences were basecalled using Dorado version 0.7.3 with the Super Accurate model v5.0.0 and a minimum Q score of 10. Briefly, sequences were first demultiplexed for the Nanopore barcode and the Nanopore barcodes were trimmed using the in-built Dorado tools. DNA sequences were then processed through a QIIME 2 bioinformatics pipeline for metagenomics. DNA sequences were size-filtered to keep only fragments between 160 and 200 bp. A first closed-reference mapping was performed to identify the "run barcode". For reads which validated the correct run barcode, a second closed-reference mapping

was performed against the 123 potential STAMP tags to calculate the tag abundances. Three tags exogenous tags (namely tag121, tag122, tag123) were used to calibrate barcode hopping. Barcode hopping was estimated by measuring the hopping between the 120 STAMP tags from samples toward the three control tags. A typical order of magnitude of $\sim 1\%$ of noise reads was obtained for final depths of sequencing of $> 10^4$ reads in all samples.

4.5 N_b-derived indicators calculation and improvements of the STAMPR pipeline

For the calculation of the N_b, N_r and N_s metrics, the code from the original STAMPR pipeline[2] was adapted. In short, the code was corrected to include the "resiliency algorithm" method and the calculation of N_r in addition to N_s (see below). We also included additional error estimators during the calculation of N_b and N_r.

As part of the pipeline, we set the prefiltering threshold to remove noise tags at 25 or fewer reads. This threshold was selected based on the estimation of barcode hopping in our experimental setup. This threshold corresponds to a threshold to filter out at least quantile 99% of tags emerging from noise alone.). Eliminated tags typically accounted for less than 1% of tag abundance in samples and less stringent thresholds had minimal change on N_b and N_r.

The standard bottleneck N_b was calculated based on the analytical equation formalised in the original STAMP publication[1] using the prefiltered data:

$$N_b = \frac{g}{\left(\frac{1}{K}\sum_{i=1}^{K}\frac{(f_i - f_i^0)^2}{f_i^0(1-f_i^0)} - \frac{1}{S_0} - \frac{1}{S_s}\right)}, \tag{1}$$

with K the number of tags in inoculum, f_i^0 and f_i the frequencies of tag i respectively in inoculum and sample, $g = 1$ the number of generation, S_0 and S_s the sequencing depths respectively in inoculum and sample. The limit of detection of the N_b metric was calculated in our experiment by considering a signal-to-noise problem. Noise was considered to be the sum of technical artefacts in tag abundances originating from PCR noise, residual barcode hopping or misattribution of tags during bioinformatic analysis. An artefactual N_b was calculated between technical replicate of sequencing of a same inoculum. $N_b > 4 \times 10^3$ was obtained indicating that it is not possible to discriminate values of N_b above this threshold.

A corrected bottleneck value N_r was derived from N_b. The original code of the STAMPR pipeline[2] was cleaned and annotated. Previously, only calculation of N_s was made available based on the "reference resample plot" of the algorithm. Instead, we corrected the code so that both N_s and N_r are systematically computed. Finally, an algorithm was added to estimate whether the number of tags in the inoculum is sufficient to accurately estimate a N_b or N_r. This algorithm is similar to the simulations that were performed in the original STAMP publication[1]. The algorithm simulates bottleneck events under the estimated N_b or N_r and the resulting standard deviation provides the

confidence interval in the calculation of a given N_b or N_r.

4.6 Measuring diversity in samples and model comparison

In this section, we construct a method to compare the observed data with the data generated by mechanistic models (see Section 4.7). This method allows us (i) to estimate the parameters of our models and (ii) to compare the ability of our models to reproduce the observed data.

Hill numbers and Hill curve. Our comparison methods is based on the Hill numbers. The Hill number of order q of a frequency vector $F^1 = (f_1, \ldots, f_K)$ is defined as:

$$^qH = \left(\sum_{i=1}^{K} (f_i)^q \right)^{\frac{1}{1-q}}.$$

Certain values of q correspond to standard diversity indices: ^0H represents species richness (number of types); ^1H corresponds to the exponential of Shannon diversity index; ^2H is related to the inverse Simpson diversity index, giving more weight to common tags. For all values of q, the maximum value of ^qH is reached when $f_i = 1/K$ for all i. In this case, $^qH = K$. More generally, for each fixed q, a lower ^qH corresponds to lower diversity, and the parameter q controls the relative emphasis placed on common tags (large q) or rare tags (small q).

As proposed in reference[26], we describe the distribution of the frequencies through the full *diversity profile* ^qH over a continuum of values of q. The reason for this choice is that the diversity profile fully characterises the frequencies (proposition A22 of reference[26]), as two frequency vectors cannot lead to the same profile unless they are equal up to a permutation.

Models and data comparison. Observing the Hill curves allows us to directly visualise the effect of the bottleneck on the frequency distribution. These profiles also allow us to compare models and data. Consider two frequency vectors $F^1 = (f_1^1, \ldots, f_K^1)$ and $F^2 = (f_1^2, \ldots, f_K^2)$. We define the discrepancy between these frequencies as the average relative difference between the Hill numbers of the two vectors over a range of q values:

$$d(F_1, F_2) = \frac{1}{\#Q} \sum_{q \in Q} \frac{|^qH(F_1) - {}^qH(F_2)|}{^qH(F_1) + {}^qH(F_2)},$$

where Q is a representative set of values of q, and $\#Q$ is the number of elements in this set. We took Q to be a set of evenly spaced values ranging from 0 to 4. This range was empirically selected as experimental data typically showed the highest variations on the interval $[0, 4]$.

Now, consider a stochastic model $\mathcal{M}(\theta)$, parametrised by $\theta \geq 0$, and describing the distribution of the frequencies F after the bottleneck event. Given the observed experimental frequencies $\hat{F}$, for each fixed θ, we define the performance $P[\mathcal{M}(\theta)]$ of $\mathcal{M}(\theta)$ as the 0.05 quantile of the distribution of $d(F, \hat{F})$ over replicate simulations. Then, the performance $P[\mathcal{M}]$ of the model $\mathcal{M}$ is obtained by choosing the parameter θ that leads to the smallest value of $P[\mathcal{M}(\theta)]$. The model is more effective in reproducing $\hat{F}$

when $P[\mathcal{M}]$ is small. In other words, we let $P[\mathcal{M}(\theta)]$ be the 0.05 quantile of

$$\left\{d(F_i[\mathcal{M}(\theta)], \hat{F}),\ i = 1, \ldots, N\right\}$$

where $F_i[\mathcal{M}(\theta)] \in [0,1]^K$, $i = 1, \ldots, N$, are the final frequencies for N replicate simulations simulated with model $\mathcal{M}$ and parameter θ. We then let

$$P[\mathcal{M}] := \min_{\theta} P[\mathcal{M}(\theta)], \qquad \theta[\mathcal{M}] := \operatorname*{argmin}_{\theta} P[\mathcal{M}(\theta)],$$

be, respectively, the performance of the model $\mathcal{M}$ and the estimated parameter for the model $\mathcal{M}$.

In our situation, we have several experimental frequency vectors $\hat{F}_1$, ..., $\hat{F}_N$, observed under the same experimental conditions. We consider independently the vectors $\hat{F}_1$, ..., $\hat{F}_N$. For $i = 1, \ldots, N$, let θ_i be the parameter that leads to the smallest value of $P[\mathcal{M}(\theta_i); F_i]$. The model performance is then the average of the $P[\mathcal{M}(\theta_i); F_i]$, $i = 1, \ldots, N$, and the output parameter $\widehat{\theta}$ is the average of the θ_i.

4.7 Mechanistic Models

We propose four stochastic mechanistic models that describe different ways of crossing the barrier. Comparing the performance of these models allows us to select the best one and infer the most probable underlying mechanism. For each model $\mathcal{M}(\theta)$, the parameter θ determines the intensity of the bottleneck. In all models, the smaller the value of θ, the stronger the bottleneck effect (however, θ may scale differently according to the model).

Instantaneous bottleneck model $\mathcal{M}_{\text{STAMP}}(\theta_{\text{STAMP}})$. This is the standard model derived from the original STAMP publication[1]. From a mechanistic perspective, the model assumes that the founding population after the bottleneck consists of N bacteria that cross a barrier simultaneously. These individuals are randomly selected from the initial population according to a multinomial distribution:

$$\mathcal{M}_{\text{STAMP}}(\theta_{\text{STAMP}}): \quad F \sim \text{Multinomial}(N; F_0)/N, \tag{2}$$

where F_0 represents the pre-bottleneck frequencies and F stands for the post-bottleneck frequencies. The parameter of the model is the size of the founding population: $\theta_{\text{STAMP}} = N$. It can be determined as the value θ^*_{STAMP} that maximises the performance $P[\mathcal{M}_{\text{STAMP}}(\theta_{\text{STAMP}})]$ or approximated analytically using the estimator:

$$\hat{\theta}_{\text{STAMP}} = \frac{1}{K} \sum_{i=1}^{K} \frac{(F_i - F_i^0)^2}{F_i^0(1 - F_i^0)},$$

based on Eq. (1). However, this formula is only applicable when F follows (2). Significant discrepancies from the value of θ_{STAMP} obtained by maximising performance may appear when F does not follow a multinomial distribution.

Constant rate model $\mathcal{M}_{\mathrm{CR}}(\theta_{\mathrm{CR}})$. Bacteria cross the barrier individually and stochastically at a Poisson rate $\mu > 0$, carrying tags selected according to F_0, the pre-barrier frequencies. Once across the barrier, bacteria reproduce deterministically following Malthusian growth at rate r. Under those assumptions, the output $X_t = (x_1(t), \ldots, x_K(t))$ represents the number of bacteria carrying each tag at time t. By the properties of Poisson point processes, this is equivalent to assuming that

$$x_i(t) = \sum_{j \geq 1} 1_{\{\tau_{i,j} \leq t\}} \, e^{r\tau_{i,j}}, \tag{3}$$

where, for each $i \in \{1, \ldots, K\}$, $\{\tau_{i,j}, j \geq 1\}$ are the points of a Poisson process with intensity μ/K, and these processes are mutually independent. The corresponding frequencies depend on the observation time and are given by $F_t = X_t/n_t$, where $n_t = \sum x_i(t)$. The parameter of the constant-rate model is defined as $\theta_{\mathrm{CR}} = \mu/r$. It quantifies the relative entry rate of bacteria through the bottleneck compared to their Malthusian growth rate. We interpret θ_{CR} as a measure of bottleneck strength: high θ_{CR} ($r \ll \mu$) means that bacteria cross the bottleneck relatively quickly compared to their growth, making the final population composition closer to the pre-bottleneck distribution. Conversely, low θ_{CR} ($r \gg \mu$) means that bacteria grow much faster than they cross the bottleneck. Early crossers dominate, as they have more time to expand before new bacteria enter, leading to a founder effect where the first few individuals disproportionately shape the post-bottleneck population structure.

Bolthausen-Sznitman model $\mathcal{M}_{\mathrm{BS}}(v)$. To construct the Bolthausen–Sznitman model, we assume that the population is described by a Fisher-KPP equation. The Fisher–KPP equation is a reaction–diffusion equation commonly used to model population dynamics, particularly the evolution of neutral tags during a spatio-temporal expansion process[37] occurring at a constant propagation speed. To account for finite-population effects, we introduce stochasticity, leading to a noisy Fisher–KPP equation.

We see the bottleneck as an area where the population must remain very small, and outside of which the population is large. In the experiment, n individuals are sampled shortly after the population has crossed the barrier. *What are their genealogies?* No common ancestor can be found outside the barrier, since the population is large in these areas. However, inside the barrier, common ancestors can be found. The connection to our problem is that if two individuals located after the barrier are sampled, then they will necessarily carry the same tag if they have a common ancestor that lived after the tags were attributed. If no such common ancestor exists, the tags of the two sampled individuals are independent. Similarly, if we know the genealogies of a sample of $n \geq 3$ individuals, then we perfectly know the joint law of their tags. Therefore, understanding how the genealogies of individuals are affected by the crossing of the barrier is sufficient to understand the frequencies of the different tags that we observe at sampling time.

There exist different standard population genetics models for such genealogies. We tested two of them, the Kingman coalescent and the Bolthausen-Sznitman coalescent, which are conjectured or

shown to arise in various forms of the noisy Fisher-KPP equations[25,38,39]. We do not show the Kingman coalescent results in the main material, as it was unable to reproduce diversity profiles similar to the experimental ones (Fig. S6, S8). In Section 4.8, we provide a construction of the Kingman coalescent and the Bolthausen-Sznitman coalescent.

The strength of the barrier in this model is measured by the time T during which the coalescent process is run to obtain the genealogy of the individuals following the bottleneck, which can be interpreted as the time taken by the population to cross the barrier. We parametrise the model with the speed $\theta_{\mathrm{BS}} = 1/T$. A high θ_{BS} means that the population crosses the barrier rapidly, so that the bottleneck is weak.

Increasing rate model $\mathcal{M}_{\mathrm{IR}}(\mu/r)$. Inspired by the Bolthausen–Sznitman model, the increasing rate model offers a simpler mechanistic interpretation while still capturing a similar behaviour in terms of arrival-time profiles (Fig. S5). Conceptually, $\mathcal{M}_{\mathrm{IR}}$ is a generalisation of the constant-rate model $\mathcal{M}_{\mathrm{CR}}$, in which the entry rate μ in the root is replaced by an increasing time-dependent rate function $\lambda(t)$, leading to a non-homogeneous Poisson process. Once across the barrier, bacteria again reproduce deterministically following Malthusian growth at rate r. Equation (3) thus remains unchanged, but the $\{\tau_{i,j}, j \geq 1\}$ are now the points of an inhomogeneous Poisson point process on $\mathbb{R}_+$ with intensity $t \mapsto \lambda(t)$.

To maintain consistency with the observed arrival-time profiles in the Bolthausen–Sznitman model, we define the rate as

$$\lambda(t) = \mu\, e^{krt},$$

with $k = 0.78$. This value was chosen because it yields the closest match between the arrival-time distributions produced by the $\mathcal{M}_{\mathrm{IR}}$ model and those observed in the Bolthausen–Sznitman model, even though the underlying parameter values differ between the two models (see Fig. S5). This exponential increase in the entry rate over time reflects a progressively intensifying inflow of individuals through the barrier. We also make this choice in order to avoid introducing an additional parameter in the model, to simplify the comparison with other models. The scaling factor rt ensures that the frequencies produced by this model remain independent of the Malthusian growth rate r.

To clarify this point, consider the non-homogeneous Poisson process with intensity

$$\lambda_s(t) = s\,\frac{\mu}{r}\,e^{kst}.$$

In this process, the arrival time $t_{i,s}$ of the ith bacterium is proportional to $1/s$, that is, $t_{i,s} = t_{i,1}/s$. Therefore, the relative frequency of the $(i+1)$th bacterium to the ith is

$$\begin{aligned}\frac{x_{i+1,s}}{x_{i,s}} &= \exp\left[r(t_{i+1,s} - t_{i,s})\right] \\ &= \exp\left[\frac{r}{s}(t_{i+1,1} - t_{i,1})\right].\end{aligned}$$

Thus, with the crossing intensity $\lambda_s(t)$ and Malthusian growth rate r, the relative frequencies are the same as with the crossing intensity $\lambda_1(t)$ and growth rate r/s. Taking the scaling factor $s = r$, we see that the model with crossing intensity $\lambda(t)$ and growth rate r is equivalent, in terms of frequencies, to the model with crossing intensity

$$\lambda_1(t) = \frac{\mu}{r}\, e^{kt}$$

and growth rate 1.

Hence, as in the $\mathcal{M}_{\mathrm{CR}}$ model, only the ratio μ/r is identifiable from the observed frequencies F. Consequently, we arbitrarily fix $r = 1$ and $t = 10$, and determine the value $\theta^*_{\mathrm{IR}} = (\mu/r)^*$ that maximises the performance $P[\mathcal{M}_{\mathrm{IR}}(\theta_{\mathrm{IR}} = \mu/r)]$.

Summary of the models.

- In $\mathcal{M}_{\mathrm{STAMP}}(\theta_{\mathrm{STAMP}} = N_b)$, the founding population after the bottleneck consists of exactly θ_{STAMP} bacteria that cross the barrier simultaneously, selected from the initial population according to a multinomial distribution, leading to a stronger founder effect as θ_{STAMP} decreases.

- In $\mathcal{M}_{\mathrm{CR}}(\theta_{\mathrm{CR}} = \mu/r)$, bacteria cross the bottleneck stochastically at a Poisson rate μ and then grow exponentially at rate r. The ratio $\theta_{\mathrm{CR}} = \mu/r$ characterises the strength of the bottleneck: a low θ_{CR} results in strong founder effects and reduced diversity.

- In $\mathcal{M}_{\mathrm{BS}}(\theta_{\mathrm{BS}})$, bottleneck crossing is modelled as a stochastic propagation process, where the parameter θ_{BS} corresponds to the speed at which the population crosses the bottleneck. A lower speed θ_{BS} increases the amount of coalescence, leading to a stronger bottleneck effect.

- In $\mathcal{M}_{\mathrm{IR}}(\theta_{\mathrm{IR}} = \mu/r)$, the bottleneck is crossed at a time-inhomogeneous rate $\lambda(t) = \frac{\mu}{r} e^{kt/r}$, leading to progressively more frequent entries as time increases. Bacteria then grow exponentially at rate r. This variable-rate mechanism generalises the constant entry rate model $\mathcal{M}_{\mathrm{CR}}$ and reproduces arrival profiles similar to those of the $\mathcal{M}_{\mathrm{BS}}$ model. The parameter $\theta_{\mathrm{IR}} = \mu/r$ again governs the bottleneck strength, with smaller values indicating a stronger founder effect.

4.8 Description of the Kingman and Bolthausen-Sznitman coalescents

The Kingman coalescent. The Kingman coalescent is an object that follows the genealogy of current individuals. Let n current individuals be labelled by $1, \ldots, n$. The n-Kingman coalescent is a process going backward in time, which, at time t, contains the ancestors of the n current individuals living at time t *before* the present time. More specifically:

1. The initial state, denoted by Π_0, is the set of blocks $\{1\}, \ldots, \{n\}$. Each block corresponds to a single individual living at the present time;

2. Each $t > 0$ corresponds to a time *in the past*. Then Π_t is made of blocks of families of individuals living at the present time. For example, if $\Pi_t = \{1, 2\}, \{3\}, \{4\}$, this means that individuals

1 and 2 share a common ancestor that lived at time $-t$; and 3 and 4 do not share a common ancestor with $1, 2$ that lived at this time;

3. The dynamics of Π_t is as follows: any given pair of blocks merges at rate 1. For example, at rate 1, $\{1, 2\}$ and $\{3\}$ will try to merge to form $\{1, 2, 3\}$. A merger at time t means that the two families have found their most recent common ancestor at time t before present.

The Bolthausen-Sznitman coalescent. The Bolthausen-Sznitman coalescent, similarly to the Kingman coalescent, is a process that goes backward in time and that, at time t, regroups individuals who share a common ancestor at time t *before* the present time. However, the mechanism for the merging of blocks is different from that of the Kingman coalescent. While in the Kingman coalescent, only two blocks can merge at the same time, the Bolthausen-Sznitman coalescent allows *multiple mergers*. There are several constructions of the Bolthausen-Sznitman coalescent. It can be seen as the Λ-coalescent with $\Lambda(dx) = dx$[40]. However, we define it here in another way, which is apter to simulations, using the construction of[41] (see also the description in[40]). First, construct a tree recursively in the following way. The root is indexed by 1. Once n vertices are positioned on the tree, the $(n+1)^{th}$ vertex chooses its parent uniformly at random among the n vertices of the tree. Each vertex of the tree corresponds to a block; initially, all blocks contain only a singleton.

The merging procedure is as follows. Each edge of the tree carries an exponential clock with rate 1. If the clock of an edge rings, the edge is "lifted"; namely, all descendants of the edge are absorbed by the parent of the edge. The procedures goes on until there is only one vertex left (see Fig. S10).

4.9 Estimation of μ and r using the constant rate or increasing rate models

We consider here the models $\mathcal{M}_{\mathrm{CR}}$ and $\mathcal{M}_{\mathrm{IR}}$. The growth rate is estimated as follows. For each sample, we measure the bacterial population associated with the first arrival as $f_1 \times$ (bacterial load), where f_1 is the proportion of the majority tag. Assuming Malthusian growth with rate r, this population size equals $e^{r(t-t_1)}$, where t is the observation time and t_1 is the arrival time of the first tag under the model. For the model $\mathcal{M}_{\mathrm{CR}}$, we use $t_1 \approx E[t_1] = 1/\mu = 1/(r\theta)$. For the model $\mathcal{M}_{\mathrm{IR}}$, we approximate t_1 by the median value of the first arrival time, that we compute as follows. We use the cumulative intensity function:

$$\Lambda(t) = \int_0^t \lambda(s)\, ds = \mu \cdot \frac{e^{krt} - 1}{kr}.$$

The cumulative distribution function of the first arrival time is:

$$F(t) = 1 - \exp(-\Lambda(t)).$$

The median t_{med} satisfies $F(t_{\mathrm{med}}) = 0.5$, *i.e.*,

$$\exp\left(-\mu \cdot \frac{e^{krt_{\mathrm{med}}} - 1}{kr}\right) = 0.5.$$

Thus,

$$\mu \cdot \frac{e^{krt_{\text{med}}} - 1}{kr} = \ln(2).$$

and

$$t_1 \approx t_{\text{med}} = \frac{1}{kr} \ln\left(1 + \frac{kr}{\mu} \ln(2)\right) = \frac{1}{kr} \ln\left(1 + \frac{k}{\theta} \ln(2)\right).$$

We then approximate r using the formula:

$$r \approx \frac{\ln(f_1 \times \text{bacterial load})}{t - t_1}.$$

For the model $\mathcal{M}_{\text{CR}}$, this leads to

$$r_{\text{CR}} \approx \frac{\ln(f_1 \times \text{bacterial load}) + \frac{1}{\theta}}{t}.$$

For the model $\mathcal{M}_{\text{IR}}$, we get:

$$r_{\text{IR}} \approx \frac{\ln(f_1 \times \text{bacterial load}) + \frac{1}{k} \ln\left(1 + \frac{k}{\theta} \ln(2)\right)}{t}.$$

References

[1] Sören Abel, Pia Abel zur Wiesch, Hsiao-Han Chang, Brigid M. Davis, Marc Lipsitch, and Matthew K. Waldor. STAMP: Sequence tag-based analysis of microbial population dynamics. *Nature methods*, 12(3):223, 2015. doi: 10.1038/nmeth.3253. Publisher: NIH Public Access.

[2] Karthik Hullahalli, Justin R Pritchard, and Matthew K Waldor. Refined quantification of infection bottlenecks and pathogen dissemination with STAMPR. *MSystems*, 6(4):10–1128, 2021.

[3] Anel Mahmutovic, Aaron Nicholas Gillman, Silje Lauksund, Natasha-Anne Robson Moe, Aime Manzi, Merete Storflor, Pia Abel zur Wiesch, and Sören Abel. RESTAMP – Rate estimates by sequence-tag analysis of microbial populations. *Computational and Structural Biotechnology Journal*, 19:1035–1051, January 2021. ISSN 2001-0370. doi: 10.1016/j.csbj.2021.01.017.

[4] Ting Zhang, Sören Abel, Pia Abel Zur Wiesch, Jumpei Sasabe, Brigid M. Davis, Darren E. Higgins, and Matthew K. Waldor. Deciphering the landscape of host barriers to Listeria monocytogenes infection. *Proceedings of the National Academy of Sciences of the United States of America*, 114(24):6334–6339, June 2017. ISSN 1091-6490. doi: 10.1073/pnas.1702077114.

[5] Kelly E. R. Bachta, Jonathan P. Allen, Bettina H. Cheung, Cheng-Hsun Chiu, and Alan R. Hauser. Systemic infection facilitates transmission of Pseudomonas aeruginosa in mice. *Nature Communications*, 11(1):543, January 2020. ISSN 2041-1723. doi: 10.1038/s41467-020-14363-4. Publisher: Nature Publishing Group.

[6] Xue Liu, Jacqueline M. Kimmey, Laura Matarazzo, Vincent de Bakker, Laurye Van Maele, Jean-Claude Sirard, Victor Nizet, and Jan-Willem Veening. Exploration of bacterial bottlenecks and Streptococcus pneumoniae pathogenesis by CRISPRi-seq. *Cell host & microbe*, 29(1):107–120.e6, January 2021. ISSN 1931-3128. doi: 10.1016/j.chom.2020.10.001.

[7] Sarah E Woodward, Stefanie L Vogt, Jorge Peña-Díaz, Ryan A Melnyk, Mihai Cirstea, Antonio Serapio-Palacios, Laurel M P Neufeld, Kelsey E Huus, Madeline A Wang, Cara H Haney, and B Brett Finlay. Gastric acid and escape to systemic circulation represent major bottlenecks to host infection by Citrobacter rodentium. *The ISME Journal*, 17(1):36–46, January 2023. ISSN 1751-7362. doi: 10.1038/s41396-022-01321-9.

[8] Aaron Nicholas Gillman, Anel Mahmutovic, Pia Abel zur Wiesch, and Sören Abel. The Infectious Dose Shapes Vibrio cholerae Within-Host Dynamics. *mSystems*, 6(6):e00659–21, 2021. ISSN 2379-5077. doi: 10.1128/mSystems.00659-21.

[9] Bolutife Fakoya, Karthik Hullahalli, Daniel H. F. Rubin, Deborah R. Leitner, Roma Chilengi, David A. Sack, and Matthew K. Waldor. Nontoxigenic Vibrio cholerae Challenge Strains for Evaluating Vaccine Efficacy and Inferring Mechanisms of Protection. *mBio*, 13(2):e00539–22, April 2022. doi: 10.1128/mbio.00539-22.

[10] Karthik Hullahalli, Katherine G. Dailey, and Matthew K. Waldor. Innate immune responses yield tissue-specific bottlenecks that scale with pathogen dose. *Proceedings of the National Academy of Sciences*, 120(37):e2309151120, September 2023. doi: 10.1073/pnas.2309151120. Publisher: Proceedings of the National Academy of Sciences.

[11] Ian W. Campbell, Karthik Hullahalli, Jerrold R. Turner, and Matthew K. Waldor. Quantitative dose-response analysis untangles host bottlenecks to enteric infection. *Nature Communications*, 14:456, January 2023. ISSN 2041-1723. doi: 10.1038/s41467-023-36162-3.

[12] Victoria Chevée, Karthik Hullahalli, Katherine G. Dailey, Leslie Güereca, Chenyu Zhang, Matthew K. Waldor, and Daniel A. Portnoy. Temporal and spatial dynamics of Listeria monocytogenes central nervous system infection in mice. *Proceedings of the National Academy of Sciences*, 121(17):e2320311121, April 2024. doi: 10.1073/pnas.2320311121. Publisher: Proceedings of the National Academy of Sciences.

[13] Caitlyn L. Holmes, Katherine G. Dailey, Karthik Hullahalli, Alexis E. Wilcox, Sophia Mason, Bridget S. Moricz, Lavinia V. Unverdorben, George I. Balazs, Matthew K. Waldor, and Michael A. Bachman. Patterns of Klebsiella pneumoniae bacteremic dissemination from the lung. *Nature Communications*, 16(1):785, January 2025. ISSN 2041-1723. doi: 10.1038/s41467-025-56095-3.

[14] Marine Lebrun-Corbin, Bettina H. Cheung, Karthik Hullahalli, Katherine G. Dailey, Keith Bailey, Matthew K. Waldor, Richard G. Wunderink, Kelly E. R. Bachta, and Alan R. Hauser. Pseu-

domonas aeruginosa population dynamics in a vancomycin-induced murine model of gastrointestinal carriage. *mBio*, 16(5):e0313624, May 2025. ISSN 2150-7511. doi: 10.1128/mbio.03136-24.

[15] Julia A. Hotinger, Ian W. Campbell, Karthik Hullahalli, Akina Osaki, and Matthew K. Waldor. Quantification of Salmonella enterica serovar Typhimurium population dynamics in murine infection using a highly diverse barcoded library. *eLife*, 13:RP101388, February 2025. ISSN 2050-084X. doi: 10.7554/eLife.101388.

[16] Stefan T. Peterson, Katherine G. Dailey, Karthik Hullahalli, Daniel Sorobetea, Rina Matsuda, Jaydeen Sewell, Winslow Yost, Rosemary O'Neill, Suhas Bobba, Nicolai Apenes, Matthew E. Sherman, George I. Balazs, Charles-Antoine Assenmacher, Arin Cox, Matthew Lanza, Sunny Shin, Matthew K. Waldor, and Igor E. Brodsky. TNF signaling maintains local restriction of bacterial founder populations in intestinal and systemic sites during oral Yersinia infection. *mBio*, 0(0):e01779–25, September 2025. doi: 10.1128/mbio.01779-25. Publisher: American Society for Microbiology.

[17] Karthik Hullahalli and Matthew K Waldor. Pathogen clonal expansion underlies multiorgan dissemination and organ-specific outcomes during murine systemic infection. *eLife*, 10:e70910, 2021. ISSN 2050-084X. doi: 10.7554/eLife.70910.

[18] Marc Planas-Marquès, Jonathan P Kressin, Anurag Kashyap, Dilip R Panthee, Frank J Louws, Nuria S Coll, and Marc Valls. Four bottlenecks restrict colonization and invasion by the pathogen Ralstonia solanacearum in resistant tomato. *Journal of Experimental Botany*, 71(6):2157–2171, March 2020. ISSN 0022-0957. doi: 10.1093/jxb/erz562.

[19] Catherine Digonnet, Yves Martinez, Nicolas Denancé, Marine Chasseray, Patrick Dabos, Philippe Ranocha, Yves Marco, Alain Jauneau, and Deborah Goffner. Deciphering the route of Ralstonia solanacearum colonization in Arabidopsis thaliana roots during a compatible interaction: focus at the plant cell wall. *Planta*, 236(5):1419–1431, November 2012. ISSN 1432-2048. doi: 10.1007/s00425-012-1694-y.

[20] Marie Turner, Alain Jauneau, Stéphane Genin, Marie-José Tavella, Fabienne Vailleau, Laurent Gentzbittel, and Marie-Françoise Jardinaud. Dissection of Bacterial Wilt on Medicago truncatula Revealed Two Type III Secretion System Effectors Acting on Root Infection Process and Disease Development. *Plant Physiology*, 150(4):1713–1722, August 2009. ISSN 0032-0889. doi: 10.1104/pp.109.141523.

[21] Denise Caldwell, Bong-Suk Kim, and Anjali S. Iyer-Pascuzzi. Ralstonia solanacearum Differentially Colonizes Roots of Resistant and Susceptible Tomato Plants. *Phytopathology®*, 107(5):528–536, May 2017. ISSN 0031-949X. doi: 10.1094/PHYTO-09-16-0353-R. Publisher: Scientific Societies.

[22] Freddy Monteiro, Montserrat Solé, Irene van Dijk, and Marc Valls. A Chromosomal Insertion Toolbox for Promoter Probing, Mutant Complementation, and Pathogenicity Studies in Ralstonia solanacearum. *Molecular Plant-Microbe Interactions®*, 25(4):557–568, April 2012. ISSN 0894-0282. doi: 10.1094/MPMI-07-11-0201. Publisher: Scientific Societies.

[23] D. S. Falconer and T. F. C. Mackay. *Introduction to Quantitative Genetics*. Longmans Green, Harlow, Essex, UK, ed 4 edition, 1996.

[24] Costas B. Krimbas and Spyros Tsakas. The genetics of dacus oleae. v. changes of esterase polymorphism in a natural population following insecticide control-selection or drift? *Evolution; International Journal of Organic Evolution*, 25(3):454–460, September 1971. ISSN 1558-5646. doi: 10.1111/j.1558-5646.1971.tb01904.x.

[25] Gabriel Birzu, Oskar Hallatschek, and Kirill S. Korolev. Genealogical structure changes as range expansions transition from pushed to pulled. *Proceedings of the National Academy of Sciences*, 118(34):e2026746118, August 2021. doi: 10.1073/pnas.2026746118. Publisher: Proceedings of the National Academy of Sciences.

[26] Tom Leinster and Christina A Cobbold. Measuring diversity: the importance of species similarity. *Ecology*, 93(3):477–489, 2012.

[27] J. F. Wang, J. Olivier, P. Thoquet, B. Mangin, L. Sauviac, and N. H. Grimsley. Resistance of tomato line Hawaii7996 to Ralstonia solanacearum Pss4 in Taiwan is controlled mainly by a major strain-specific locus. *Molecular plant-microbe interactions: MPMI*, 13(1):6–13, January 2000. ISSN 0894-0282. doi: 10.1094/MPMI.2000.13.1.6.

[28] Ai Xu, Lan Wei, Jingjing Ke, Chengfeng Peng, Pengyue Li, Changqiu Fan, Xiao Yu, and Bo Li. ETI signaling nodes are involved in resistance of Hawaii 7996 to Ralstonia solanacearum-induced bacterial wilt disease in tomato. *Plant Signaling & Behavior*, 18(1):2194747, 2023. ISSN 1559-2316. doi: 10.1080/15592324.2023.2194747.

[29] Myrto Vlazaki, John Huber, and Olivier Restif. Integrating mathematical models with experimental data to investigate the within-host dynamics of bacterial infections. *Pathogens and Disease*, 77(8):ftaa001, November 2019. ISSN 2049-632X. doi: 10.1093/femspd/ftaa001.

[30] Oskar Hallatschek and David R. Nelson. Gene surfing in expanding populations. *Theoretical Population Biology*, 73(1), 2008. ISSN 00405809. doi: 10.1016/j.tpb.2007.08.008.

[31] Isai Salas-González, Guilhem Reyt, Paulina Flis, Valéria Custódio, David Gopaulchan, Niokhor Bakhoum, Tristan P. Dew, Kiran Suresh, Rochus Benni Franke, Jeffery L. Dangl, David E. Salt, and Gabriel Castrillo. Coordination between microbiota and root endodermis supports plant mineral nutrient homeostasis. *Science*, 371(6525):eabd0695, January 2021. doi: 10.1126/science.abd0695.

[32] Marie Barberon and Niko Geldner. Radial transport of nutrients: the plant root as a polarized epithelium. *Plant Physiology*, 166(2):528–537, October 2014. ISSN 1532-2548. doi: 10.1104/pp.114.246124.

[33] Marie Barberon, Joop Engelbertus Martinus Vermeer, Damien De Bellis, Peng Wang, Sadaf Naseer, Tonni Grube Andersen, Bruno Martin Humbel, Christiane Nawrath, Junpei Takano, David Edward Salt, and Niko Geldner. Adaptation of Root Function by Nutrient-Induced Plasticity of Endodermal Differentiation. *Cell*, 164(3):447–459, January 2016. ISSN 1097-4172. doi: 10.1016/j.cell.2015.12.021.

[34] Huei-Hsuan Tsai, Yuanjie Tang, Lingmin Jiang, Xiaoyan Xu, Valérie Dénervaud Tendon, Jia Pang, Yanyan Jia, Kathrin Wippel, Jordan Vacheron, Christoph Keel, Tonni Grube Andersen, Niko Geldner, and Feng Zhou. Localized glutamine leakage drives the spatial structure of root microbial colonization. *Science*, 390(6768):eadu4235, October 2025. doi: 10.1126/science.adu4235. Publisher: American Association for the Advancement of Science.

[35] Caroline Baroukh, Meriem Zemouri, and Stéphane Genin. Trophic preferences of the pathogen Ralstonia solanacearum and consequences on its growth in xylem sap. *MicrobiologyOpen*, 11(1): e1240, February 2022. ISSN 2045-8827. doi: 10.1002/mbo3.1240.

[36] Nadin Rohland and David Reich. Cost-effective, high-throughput DNA sequencing libraries for multiplexed target capture. *Genome Research*, 22(5):939–946, May 2012. ISSN 1088-9051. doi: 10.1101/gr.128124.111.

[37] L Roques, J Garnier, F Hamel, and E K Klein. Allee effect promotes diversity in traveling waves of colonization. *Proc Natl Acad Sci USA*, 109(23):8828–8833, 2012.

[38] É. Brunet, B. Derrida, A. H. Mueller, and S. Munier. Effect of selection on ancestry: An exactly soluble case and its phenomenological generalization. *Phys. Rev. E*, 76:041104, 2007. doi: 10.1103/PhysRevE.76.041104.

[39] Alison Etheridge and Sarah Penington. Genealogies in bistable waves. *Electron. J. Probab.*, 27: Paper No. 121, 99, 2022. ISSN 1083-6489. doi: 10.1214/22-ejp845.

[40] Nathanaël Berestycki. *Recent progress in coalescent theory*, volume 16 of *Ensaios Matemáticos [Mathematical Surveys]*. Sociedade Brasileira de Matemática, Rio de Janeiro, 2009. ISBN 978-85-85818-40-1.

[41] Christina Goldschmidt and James B. Martin. Random recursive trees and the Bolthausen-Sznitman coalescent. *Electron. J. Probab.*, 10:no. 21, 718–745, 2005. ISSN 1083-6489. doi: 10.1214/EJP.v10-265.

Data availability statement

All processed sequence counts and all associated metadata were kept unmodified in a all-in-one Excel data sheet available in supplementary documents. Outputs from the time-resolved analysis algorithms are conserved in a semi-controlled local environment (R project "SV_bottleneck_analysis_2024") in supplementary documents. The raw sequences data and corresponding metadata for this study have been deposited in the European Nucleotide Archive (ENA) at EMBL-EBI under accession number PRJEB102723 (https://www.ebi.ac.uk/ena/browser/view/PRJEB102723).

Code availability statement

The code for all analyses is made available in an annotated R Markdown notebook in supplementary documents. The notebook is contained in a semi-controlled local environment inside the R project "SV_bottleneck_analysis_2024" allowing to reproduce the integrality of the presented analyses, figures and statistical tests from the original data sheet (tested environment: Windows 11, RStudio, R version 4.2.2, Python version 3.11.2). The code for the processing of raw sequences data is also provided in the file "SV_nanopore_pipeline_2024" (tested environment: Shell script in Linux Ubuntu with a Conda environment, Python version 3.11.2).

Authors contribution statement

S.V. and N.P. designed the plant infection experiments. S.V. and N.P. constructed and validated the biological material. S.V., I.M. and N.P. performed the plant infection experiments. S.V. sequenced and processed the sequences data. N.B., R.F. and L.R. designed and formalised the model testing approach and the time-resolved algorithms. S.V., N.B., R.F. and L.R. wrote the code of the notebook. S.V., N.B., R.F., L.R. and N.P. discussed and analysed the data. S.V. wrote an original draft. All authors corrected and contributed to the manuscript.

Acknowledgements

The authors thank Dr. Karthik Hullahalli (ID), Dr. Kelly E. R. Bachta (ID), Dr. Michael A. Bachman (ID) for their assistance in accessing the animal infection data reanalysed in the study. The authors thank Dr. Alice Guidot (ID), Dr. Philippe Remigi and Dr. Stéphane Genin for their insightful discussions regarding the project and the manuscript. The authors thank Baptiste Mayjonade (ID) and Sandra Moreau for their assistance and the numerous insights during the establishment of Nanopore sequencing protocols.

The work of this publication was supported by the following grants. S.V. was supported by a PhD grant from the Ministère de l'Enseignement Supérieur, de la Recherche et de l'Innovation. N.P. and S.V. were supported by a seed funding "STAMP" from INRAE department Plant Health and Environment.

N.B., R.F. and L.R. were supported by the ANR project ReaCh (ANR-23-CE40-0023-01). N.B. and R.F. were supported by the Chaire Modélisation Mathématique et Biodiversité (École Polytechnique, Muséum national d'Histoire naturelle, Fondation de l'École Polytechnique, VEOLIA Environnement).

Conflicts of interest statement

The authors declare no competing interests.

Supplementary Material

Model	Average error	θ M-Intact-27	θ M-Cut-27	θ H-Cut-27	θ M-Intact-32	θ M-Cut-32	θ H-Intact-32	θ H-Cut-32
$\mathcal{M}_{\text{STAMP}}$	0.20 ± 0.01	1.00 ± 0.58	3.08 ± 1.50	2.20 ± 1.29	0.91 ± 0.54	2.65 ± 1.20	0.85 ± 0.80	2.57 ± 1.20
$\mathcal{M}_{\text{CR}}$	0.12 ± 0.01	1.00 ± 0.58	2.14 ± 0.81	1.72 ± 0.77	0.92 ± 0.53	2.17 ± 0.77	0.74 ± 0.65	2.18 ± 0.79
$\mathcal{M}_{\text{BS}}$	0.06 ± 0.01	1.00 ± 0.29	2.20 ± 0.90	2.35 ± 1.01	0.97 ± 0.37	1.98 ± 0.64	1.02 ± 0.39	1.91 ± 0.51
$\mathcal{M}_{\text{IR}}$	0.08 ± 0.02	1.00 ± 0.74	1.92 ± 0.59	1.98 ± 0.62	1.14 ± 0.60	2.11 ± 0.51	0.75 ± 0.57	2.33 ± 0.47

Table 1: Score of error (mean $\pm$ half-width of the 95% confidence interval) and mean normalised bottleneck parameter θ estimated for each infection condition from 2 and 5 (mean $\pm$ half-width of the 95% CI). Values of θ are normalised by the control condition M_Intact_27. Condition *H_Intact_27* was tolerant and did not yield sufficient colonisation to allow sequencing of the diversity and estimation of θ.

Supplementary figure 1

In vitro **growth curves for the 120 tagged strains used in study and the distribution of the estimated growth rate for each strain**

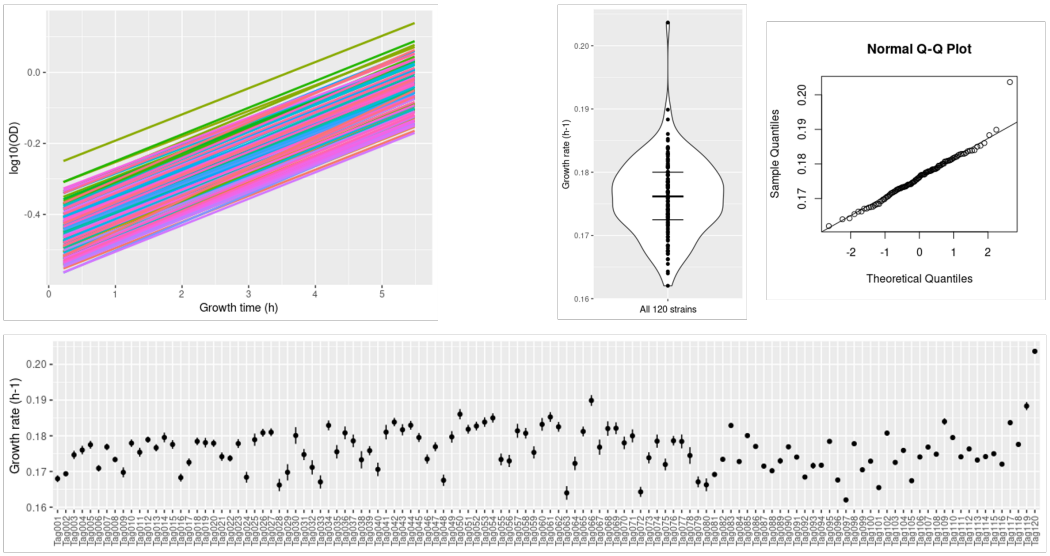

Diversity profiles in the co-cultures of the 120 tagged strains used for plant infection and distribution of each individual tag

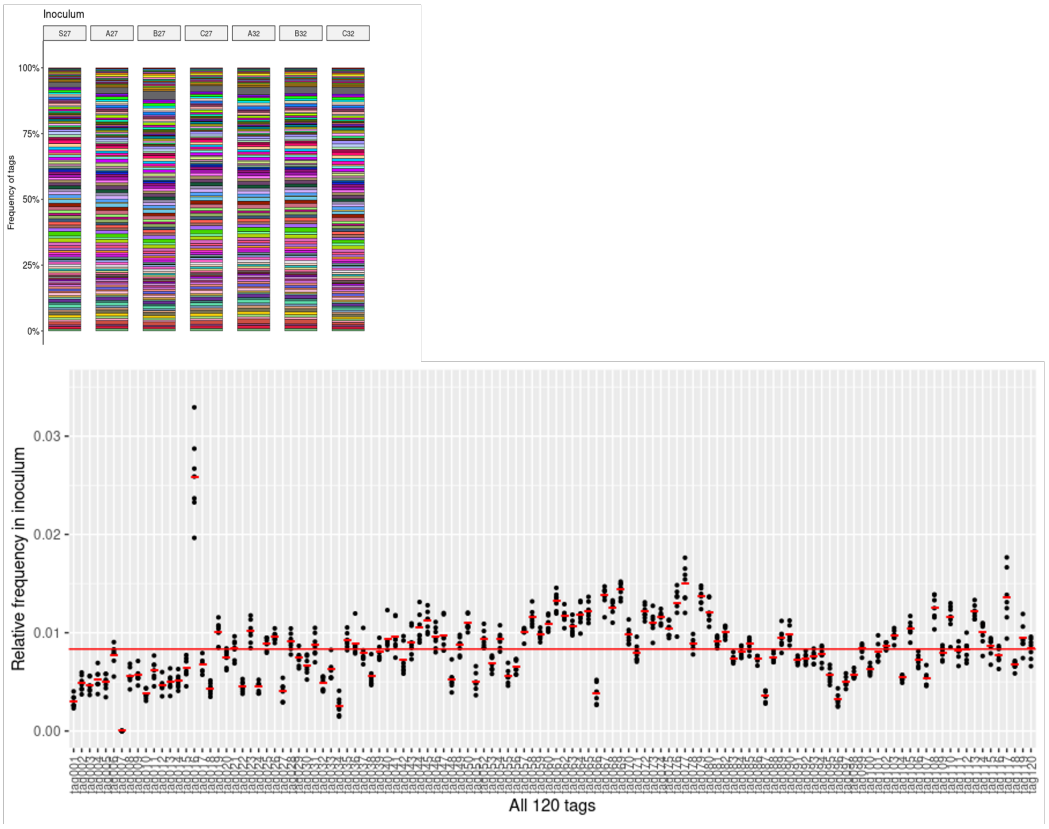

Supplementary figure S1: Technical validation of the 120-tags collection *in vitro*. The 120 tagged strains used for the constitution of co-cultures were first grown individually in microplate cultures. Each strain was monitored through OD_{600nm} and the growth curves were plotted (logarithmic scale). The distribution of the 120 growth rates was investigated in a violin plot (thick bar: median; thin bars: 1st and 3rd quartile) and in a quantile-quantile plot against a normal distribution. No important deviation from normality was visually observed suggesting a similar growth behaviour between the strains (average growth rate $r \approx 0.176h^{-1}$). Estimation of the growth rate was also individually investigated for each strain (error bars: standard deviation on the growth rate). In a second time, all co-cultures used for plant inoculation were sequenced. Visually, diversity profiles were stable across each independently prepared inoculum verifying that no technical bottlenecks were introduced at inoculum preparation. The relative frequencies at which tags appear in inocula are plotted (red bars: average across inocula; global red line: perfect frequency of 1/120). Tag007 was mistakenly forgotten from the initial pool while Tag016 was mistakenly added twice to the pool. The average frequencies did not significantly differ from the expectation of a distribution centered on a median of 1/120 (Wilcoxon-Mann-Whitney test, two-sided, $mu = 1/120$, $p = 0.74$), overall showing no indications that the 119 final tags differ in growth in co-culture.

Supplementary figure 2

Time of sampling for all tested conditions and proportion of symptomatic plants at collection time

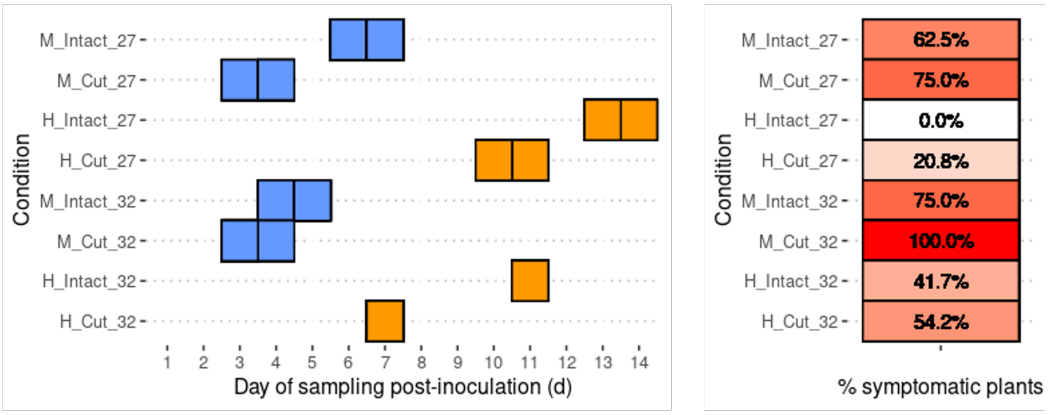

Bacterial load obtained at collection time for each condition

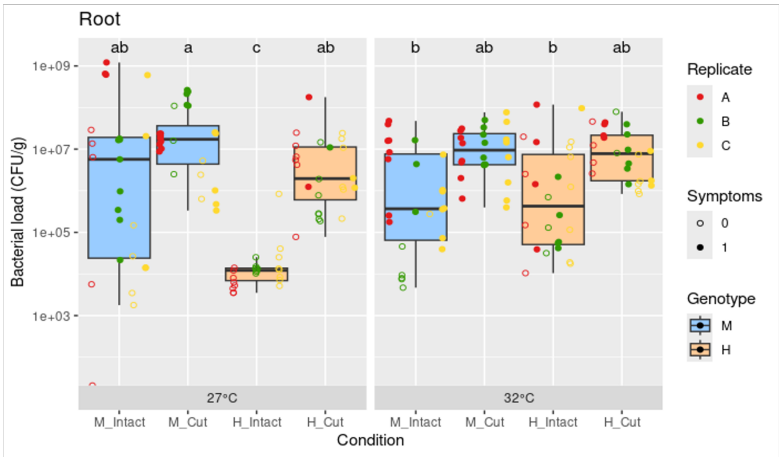

Supplementary figure S2: Day of sampling and proportion of symptomatic plants corresponding to the all conditions in Fig. 5. Conditions M_Intact_27 and M_Cut_27 correspond to the data shown in Fig. 2). At the first sign of symptoms on a batch of a replicate (replicate A, B or C), the $n = 8$ plants of the batch were collected. Batches that showed no symptoms were otherwise collected at 13-14 DPI. Bacterial load was systematically quantified. Conditions that were sampled earlier showed systematically higher or similar loads compared to conditions sampled later. Ultimately, the plants that were collected earlier also corresponded to a faster colonisation in CFU but also had faster symptoms development indicating a good representation of a gradient of susceptibility to tolerance.

Supplementary figure 3

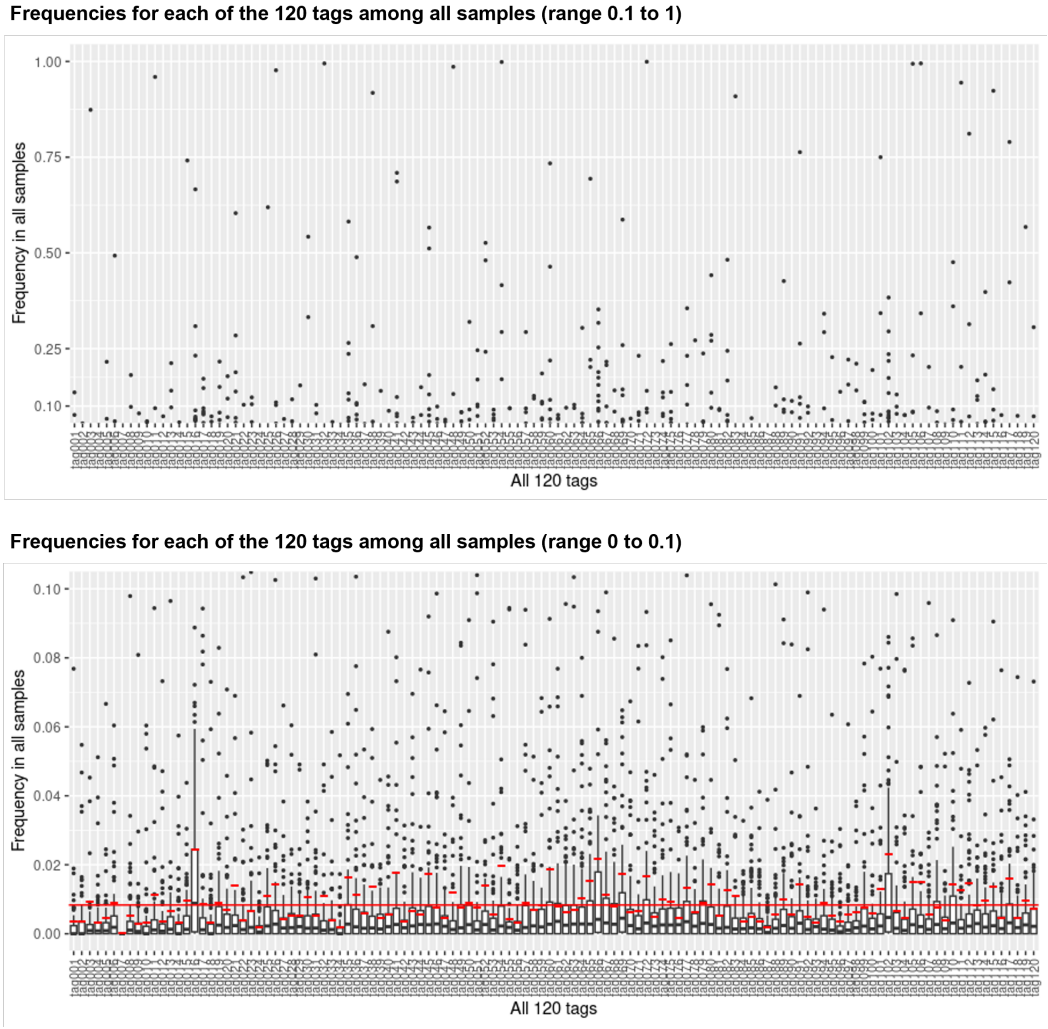

Supplementary figure S3: Technical validation of the 120-tags collection *in planta*. Relative frequencies of tags in all samples pooled from Fig. 5 including samples from Fig. 2. The frequencies are observed independently of condition (total: $n = 131$ sequenced samples on 6 time-independent infections; red bars: average frequency across samples; global red line: perfect frequency of $1/120$). For visual clarity, the frequencies are separated in two ranges (0 to 0.1 and 0.1 to 1) and the points within the boxplots are not shown. Under an expectation of neutral fitness, the frequencies averaged over a large number of events of infection should tend toward the initial inocula frequencies regardless of condition. The average frequencies did not significantly differ from the expectation of a distribution centred on a median of $1/120$ (Wilcoxon-Mann-Whitney test, two-sided, $mu = 1/120$, $p = 0.38$), overall showing no detectable difference from the assumption of neutral fitness at a collection level nor systematic sequencing bias.

Supplementary figure 4

Individual assessment of the ability of Nb and Nr to correctly explain tags richness in example samples

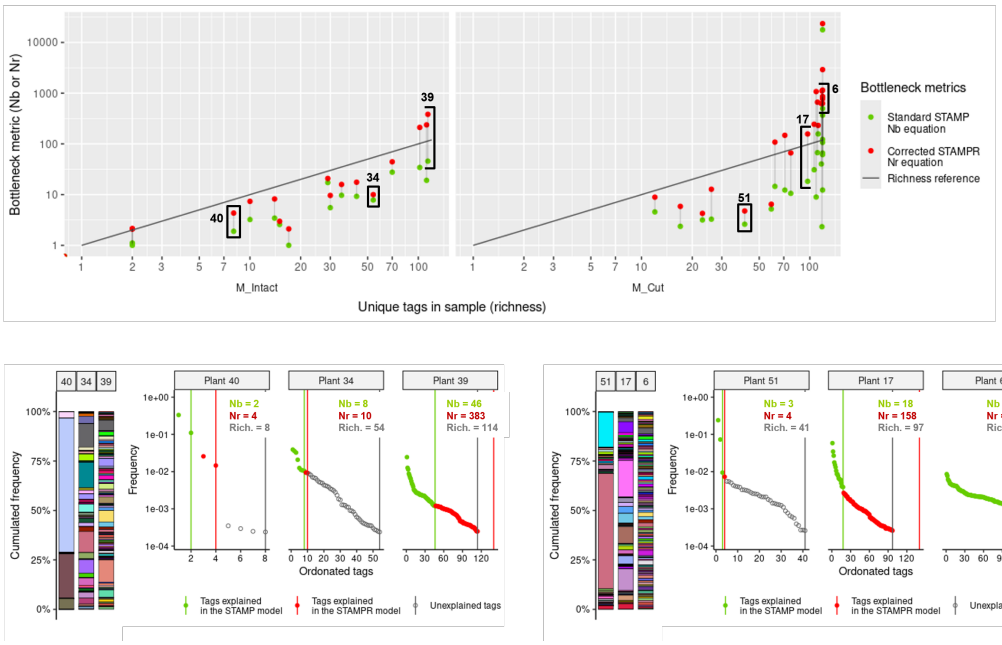

Supplementary figure S4: Assessment of the behaviour of N_b and N_r as a function of richness in sample (log-log scale). A reference line $y = x$ represents richness, values of N_b or N_r under the line are lower than richness in the same sample. A line connects N_b and N_r calculated from the same sample. Illustrative examples of diversity profiles are shown in three samples of intact Marmande plants (plants 40, 34 and 39) or three samples of root-cut Marmande plants (plants 51, 17, 6) (logarithmic scale). Tags are sorted in decreasing frequency. The green and red lines represents the number of tags that are successfully represented by N_b and N_r respectively.

Supplementary figure 5

Probability of entry of successive tags in the the four tested models

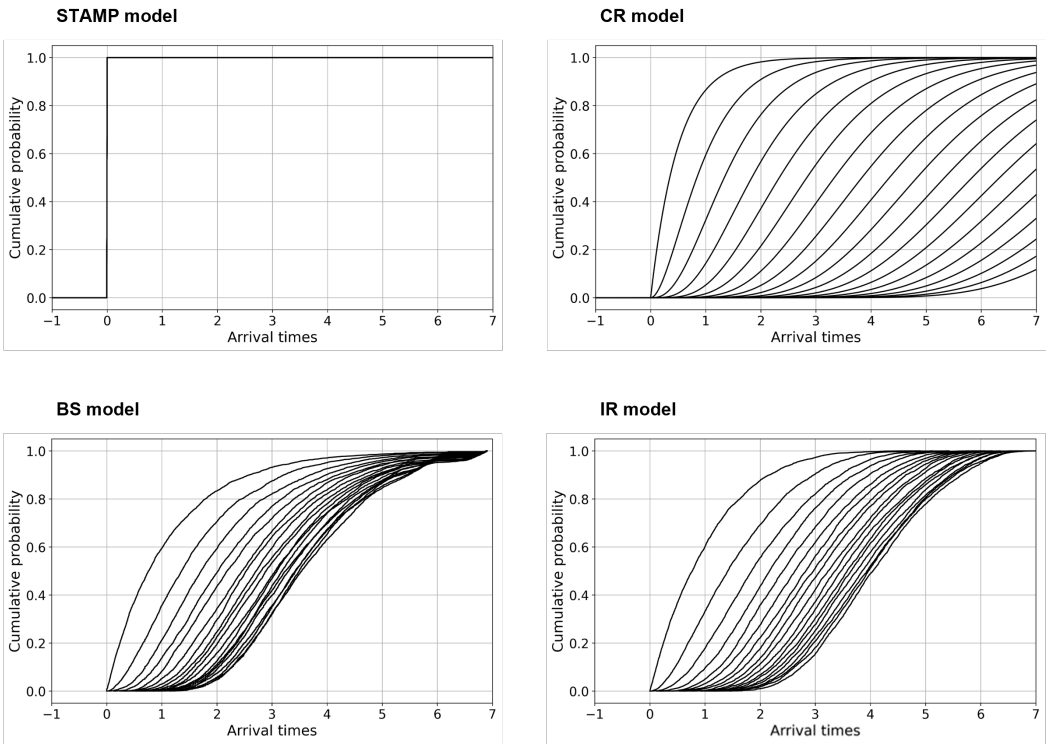

Supplementary figure S5: Comparison of arrival time distributions under the four tested models. The first bacterium enters the root at a normalised time 0. Each curve represents the Cumulative Distribution Function (CDF) of the arrival time of the kth bacterium relative to the first one. In this illustration, the parameter values are: $\mu_{\text{CR}}/r = 2$ for $\mathcal{M}_{\text{CR}}$, $v = 10$ for $\mathcal{M}_{\text{BS}}$ and $\mu_{\text{CR}}/r = 0.1$ for $\mathcal{M}_{\text{IR}}$.

Supplementary figure 6

Hill-number curves in samples and the respective best fit in each model

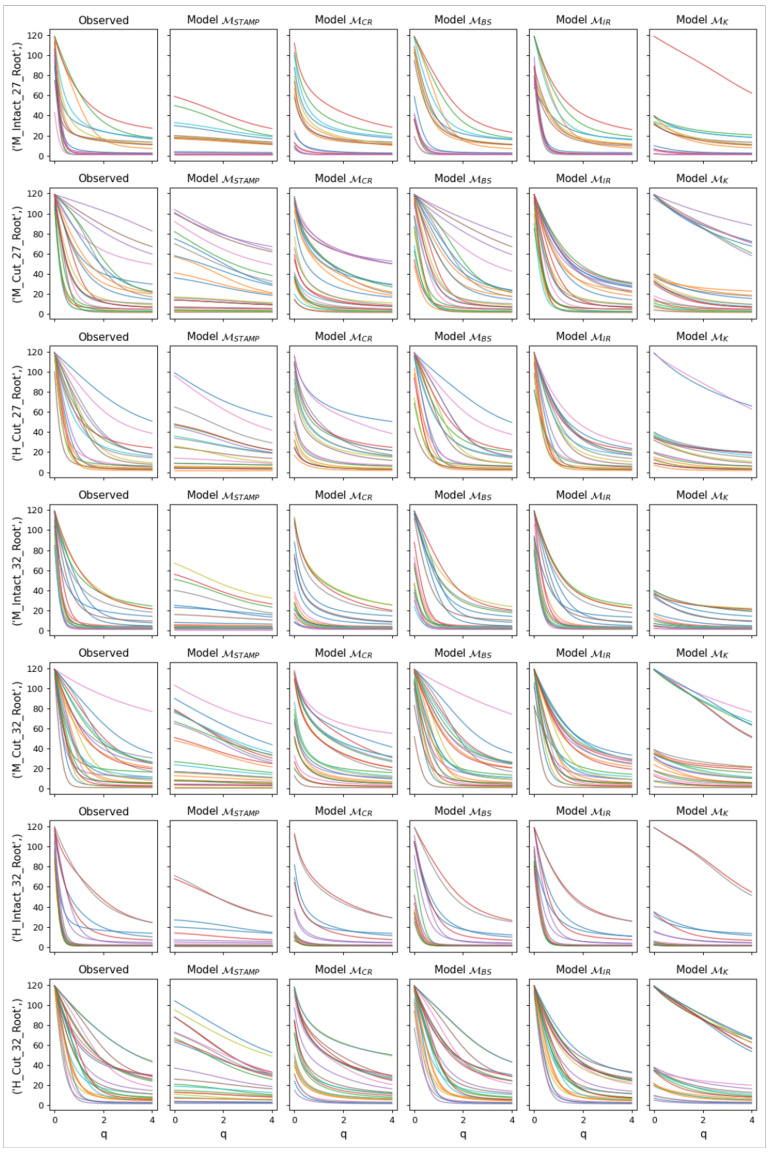

Mean relative error per condition

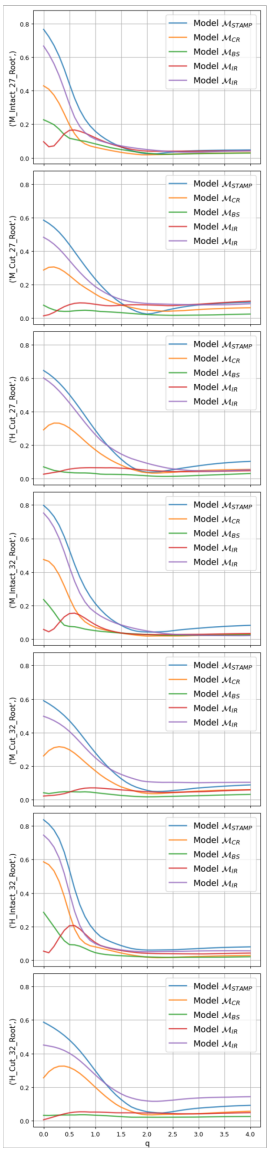

Mean relative error on all conditions

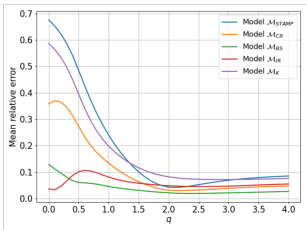

Supplementary figure S6: Diversity profiles in samples and simulations according to the Hill numbers from order $q = 0$ (giving more importance to richness) to order $q = 4$ (giving more importance to evenness). For a given order q, a high value ${}^{q}H$ indicates a high diversity. Each colour corresponds to a sample profile from Fig. 5 including those of Fig. 2. An additional model $\mathcal{M}_{\mathrm{K}}$ (Kingman model) was tested but is not presented in the main text. $\mathcal{M}_{\mathrm{K}}$ provides a simpler equation to describe biological processes of $\mathcal{M}_{\mathrm{BS}}$ but was globally unable to accurately describe the data. For each model, a score of error represents the difference between the Hill-number curve in observed data versus in best fit from a model. The error can be averaged on each condition or on all samples.

Supplementary figure 7

PERMANOVA test: contribution of all plant condition parameters to θ_{BS}

```
                     Df SumOfSqs      R2 parOmegaSq       F   Pr(>F)
`Root condition`      1   2.3786 0.16279   0.155298 28.0258 0.000999 ***
Genotype              1   0.0234 0.00160  -0.004948  0.2762 0.740260
`Temperature (°C)`    1   0.0725 0.00496  -0.000997  0.8536 0.394605
Residual            143  12.1367 0.83064
Total               146  14.6112 1.00000
---
Signif. codes:  0 '***' 0.001 '**' 0.01 '*' 0.05 '.' 0.1 ' ' 1
```

PERMANOVA test: contribution of all plant condition parameters to r_{IR}

```
                     Df SumOfSqs      R2 parOmegaSq       F   Pr(>F)
`Root condition`      1   0.2197 0.03003    0.08524  14.698 0.000999 ***
Genotype              1   4.7241 0.64577    0.68184 316.039 0.000999 ***
`Temperature (°C)`    1   0.2341 0.03200    0.09069  15.661 0.000999 ***
Residual            143   2.1375 0.29220
Total               146   7.3154 1.00000
---
Signif. codes:  0 '***' 0.001 '**' 0.01 '*' 0.05 '.' 0.1 ' ' 1
```

PERMANOVA test: contribution of collected sample weight to r_{IR}

```
                              Df SumOfSqs      R2 parOmegaSq         F   Pr(>F)
`Collected fresh weight (g)`   1   2.7285 0.37298    0.55453 183.9912 0.000999 ***
`Root condition`               1   0.2653 0.03627    0.10307  17.8923 0.000999 ***
Genotype                       1   2.1239 0.29033    0.49173 143.2182 0.000999 ***
`Temperature (°C)`             1   0.0919 0.01256    0.03415   6.1979 0.005994 **
Residual                     142   2.1058 0.28786
Total                        146   7.3154 1.00000
---
Signif. codes:  0 '***' 0.001 '**' 0.01 '*' 0.05 '.' 0.1 ' ' 1
```

PERMANOVA test: contribution of all plant condition parameters to μ_{IR}

```
                     Df SumOfSqs      R2 parOmegaSq       F   Pr(>F)
`Root condition`      1   6.8427 0.24463   0.256070 51.5991 0.000999 ***
Genotype              1   1.4379 0.05141   0.062758 10.8432 0.000999 ***
`Temperature (°C)`    1   0.7270 0.02599   0.029590  5.4823 0.008991 **
Residual            143  18.9637 0.67797
Total               146  27.9713 1.00000
---
Signif. codes:  0 '***' 0.001 '**' 0.01 '*' 0.05 '.' 0.1 ' ' 1
```

PERMANOVA test: contribution of collected sample weight to μ_{IR}

```
                              Df SumOfSqs      R2 parOmegaSq       F   Pr(>F)
`Collected fresh weight (g)`   1   1.3196 0.04718   0.057148  9.9099 0.000999 ***
`Root condition`               1   6.9936 0.25003   0.259521 52.5200 0.000999 ***
Genotype                       1   0.4143 0.01481   0.014162  3.1116 0.043956 *
`Temperature (°C)`             1   0.3351 0.01198   0.010213  2.5168 0.085914 .
Residual                     142  18.9087 0.67600
Total                        146  27.9713 1.00000
---
Signif. codes:  0 '***' 0.001 '**' 0.01 '*' 0.05 '.' 0.1 ' ' 1
```

Plot of growth rate r_{IR} in function of permeability μ_{IR}

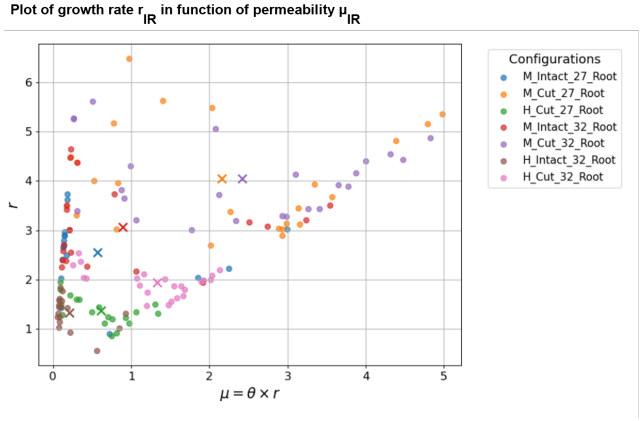

Supplementary figure S7: Output of the tests performed on the estimated parameters from Fig. 5c, 5d, 5e. Non-parametric PERMANOVA tests were performed to see the relative contribution of the three tested biological factors (*plant genotype*, *roots condition* and *temperature*) on θ_{BS}, μ_{IR} and r_{IR}. Another PERMANOVA test was performed on μ_{IR} and r_{IR} with the addition on the collected root sample weight as a proxy for a *plant size* factor. As a guide, "Pr (¿F)" and "R2" represents respectively the p-value and the coefficient of determination R^2 for each tested factor. Additionally, "parOmegaSq" represents the effect size ω^2 of each factor (> 0.1: small effect; $> 0,3$: medium effect, > 0.5 large effect). Growth rate r_{IR} was plotted in function of permeability μ_{IR}. Each cross on the graph represents the average value for each condition. Values of r_{IR} and μ_{IR} correlate positively (Spearman ranks correlation, $R^2 = 0.40$, $p = 5.97 \times 10^{-7}$)

Supplementary figure 8

Mean relative error of the five tested models in each condition of the *P. aeruginosa dataset*

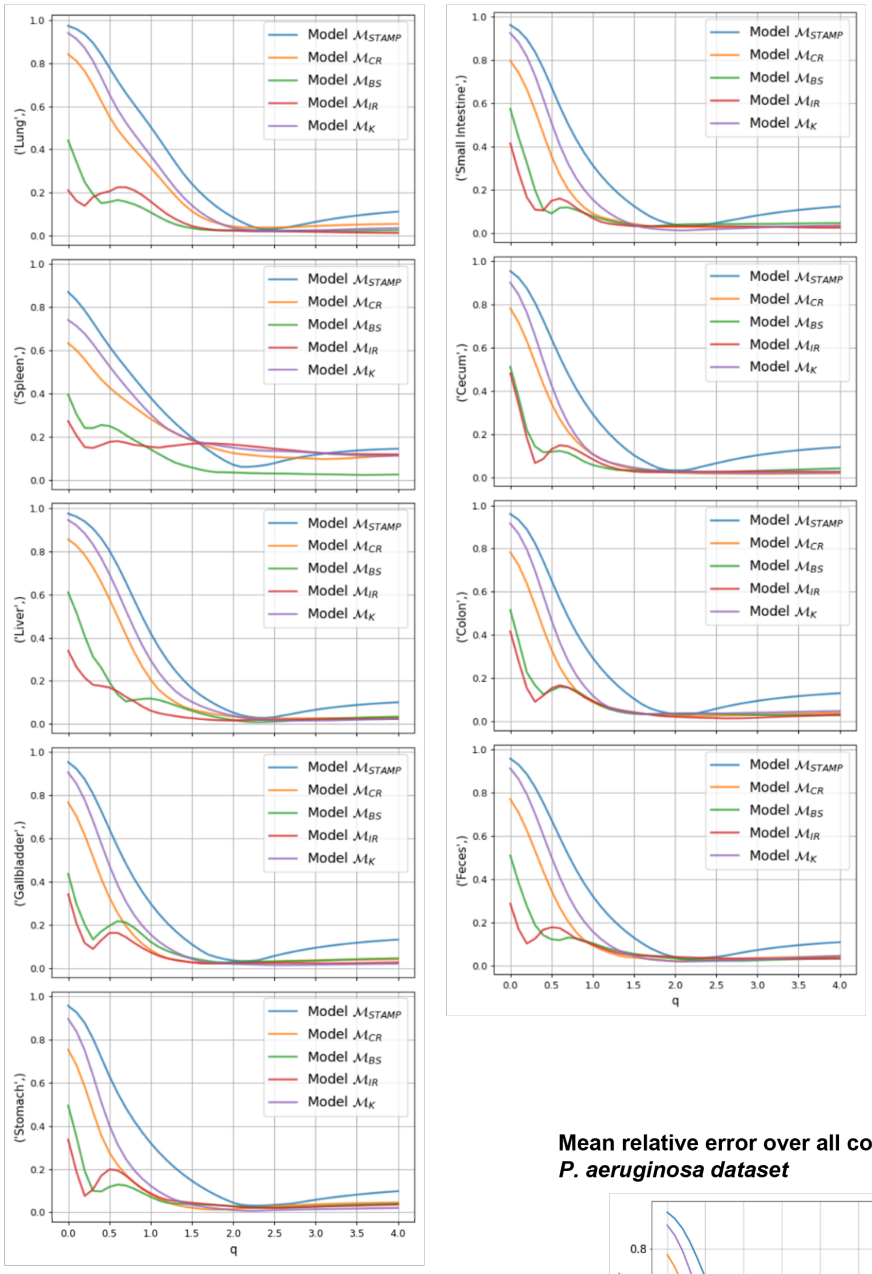

Mean relative error over all conditions of the *P. aeruginosa dataset*

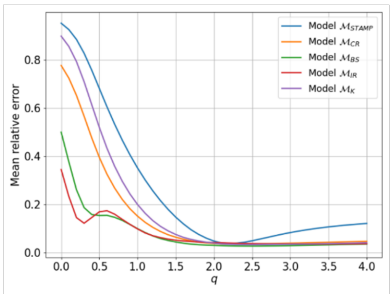

Supplementary figure S8: Score of error for the models in the range $q = 0$ to $q = 4$ on the *P. aeruginosa* infection dataset reanalysed in Fig. 6. An additional model $\mathcal{M}_{\mathrm{K}}$ (Kingman model) was tested but is not presented in the main text. $\mathcal{M}_{\mathrm{K}}$ provides a simpler equation to describe biological processes of $\mathcal{M}_{\mathrm{BS}}$ but was globally unable to accurately describe the data. For each model, a score of error represents the difference between the Hill-number curve in observed data versus in best fit from a model. The error can be averaged for each organ or on all samples.

Supplementary figure 9

Mean relative error of the models over all conditions of the *K. pneumoniae* dataset

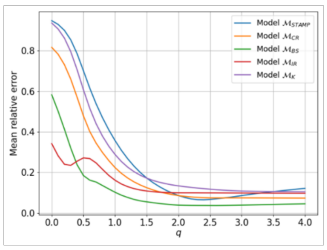

Bottleneck estimators: θ_{IR} versus N_S

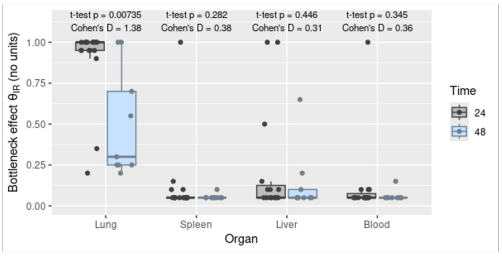

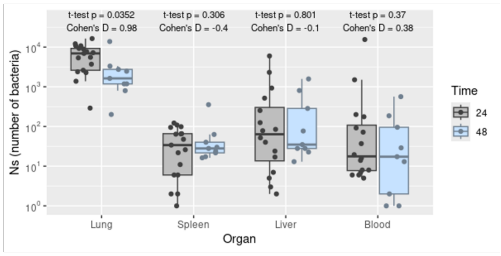

Bacterial expansion estimators: r_{IR} versus CFU/Ns and Ns/Nb

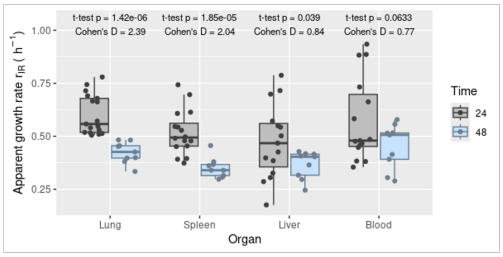

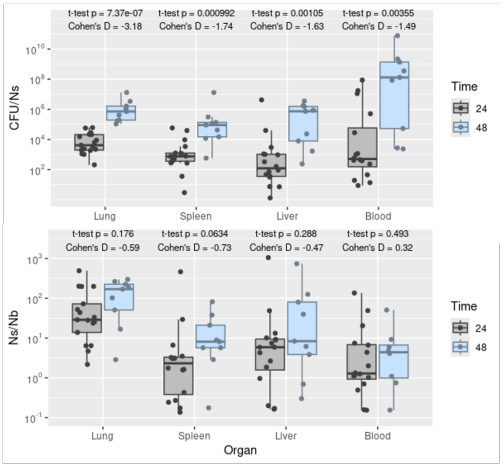

Permeability estimator: no equivalents of μ_{IR}

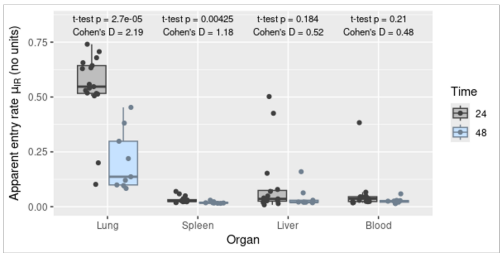

Colonisation proxy: r_{IR} versus CFU when comparing *direct* and *metastatic* disseminations in 24h samples

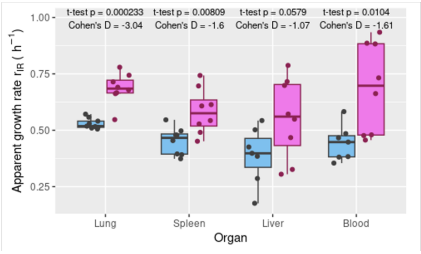

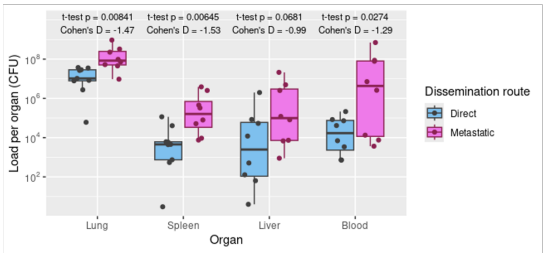

Supplementary figure S9: Time-resolved bottleneck models outperforms STAMPR at describing the dynamics of infection of *Klebsiella pneumoniae* in mice in a pneumonia infection that progresses in a bacteraemia (original data from Fig. 1 of article[13]. $n = 17$ and $n = 9$ mice were sampled at 24h and 48h respectively). The averaged score of error for the models in the range $q = 0$ to $q = 4$ showed that $\mathcal{M}_{\mathrm{BS}}$ and $\mathcal{M}_{\mathrm{IR}}$ better represented the data compared to $\mathcal{M}_{\mathrm{STAMP}}$. Model-based estimators $(\theta_{\mathrm{IR}}, \mu_{\mathrm{IR}}, r_{\mathrm{IR}})$ were compared to the closest available estimators in the STAMPR approach as follow: θ_{IR} *vs.* N_s for the bottleneck effect; r_{IR} *vs.* CFU/Ns and Ns/Nb for bacterial expansion; μ_{IR} had no equivalent for organ permeability in STAMPR. An additional comparison of r_{IR} *vs.* CFU is shown as a proxy for pathogen colonisation in the different organs in the infections characterised as *direct* or *metastatic* in the original article[13] for the mice sampled at 24 h. The performance of each estimator was assessed using two-sided Student t-test and Cohen's D effect size when comparing samples collected at 24h and 48h post-infection. For the STAMPR metrics $(N_s, CFU/N_s, N_s/N_b, CFU)$, the test was performed after logarithmic base 10 transformation of the data as in the original article[13]. Greater values of Cohen's D (positively or negatively) indicates better discrimination of the two conditions, ultimately indicating that less biological replicates are necessary to discriminates the two effects.

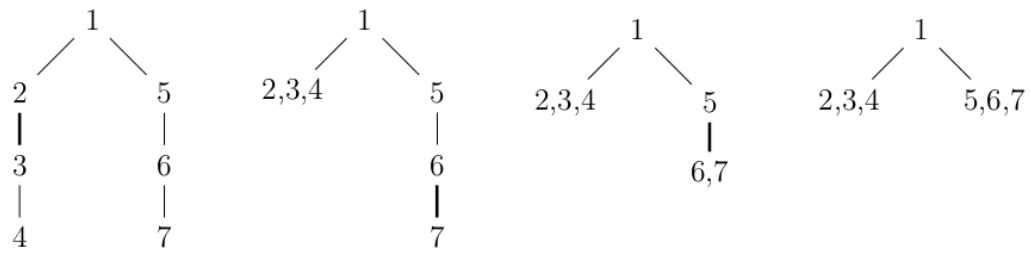

Supplementary figure S10: The construction of the Bolthausen-Sznitman coalescent of reference[41]. Each vertex corresponds to an individual. The initial tree is a random tree where the individual $n+1$ chooses its parent uniformly at random among $1, \ldots, n$. At each step, an edge (drawn thick on the picture) is lifted.